Interpretation of Net Surface Heat Fluxes and Meridional Overturning Circulations in Global Coupled HadGEM3 Climate Simulations

MICHAEL J. BELL,[a] A. J. GEORGE NURSER,[b] AND DAVID STORKEY[a]

[a] *Met Office, Exeter, United Kingdom*
[b] *National Oceanography Centre, University of Southampton Waterfront Campus, Southampton, United Kingdom*

(Manuscript received 25 March 2022, in final form 14 March 2023, accepted 16 March 2023)

ABSTRACT: The annual mean net surface heat fluxes (NSHFs) from the ocean to the atmosphere generated by historical forcing simulations using the HadGEM3-GC3.1 coupled climate model are shown to be relatively independent of resolution, for model horizontal grid spacings between 1° and 1/12°, and to agree well with those based on the DEEP-C (Diagnosing Earth's Energy Pathways in the Climate System) analyses. Interpretations of the geographical patterns of the NSHFs are suggested that use basic ideas extracted from the theory of the ventilated thermocline and planetary geostrophic layer models. As a step toward investigation of the validity of the assumptions underlying the interpretations, we examine the contributions to the rate of change of the active tracers from the main terms in their prognostic equations as a function of the active tracer and latitude. We find that, consistent with our assumptions, the main contributions from vertical diffusion occur in "near-surface" layers. We also find that, except at high latitudes, the sum of the NSHF and vertical diffusion is mainly balanced by time-mean advection of potential temperature. A corresponding statement holds for potential density but not salinity. We also show that the heat input by latitude bands is dominated by the NSHFs, the time-mean advection, and the equatorial Pacific. It is usually assumed that global integrals of tracer tendencies due to advection as a function of the tracer should be identically zero. We show that nonnegligible contributions to them arise from net freshwater surface fluxes.

SIGNIFICANCE STATEMENT: Our aim is to understand better how the heat and freshwater that are input into the ocean from the atmosphere are then redistributed within the ocean and released back into the atmosphere. We show that the geographical patterns of the heat that is input to or released from the ocean surface in coupled climate models agree well with observations. We outline a dynamically based interpretation of these surface fluxes and provide evidence that supports some of its assumptions. This work might in future help us to understand how the patterns of the surface fluxes will respond to changes in greenhouse gas forcing.

KEYWORDS: Meridional overturning circulation; Surface fluxes; Climate models

1. Introduction

Meridional overturning cells are a key component of the ocean circulation (Gordon 1986; Broecker 1991; Talley et al. 2011). How these cells are driven by surface winds and relate to surface fluxes of heat and moisture is still a very active area of research (see, e.g., Srokosz et al. 2021). These surface fluxes of heat and moisture also play an important role in driving atmospheric circulations such as the midlatitude weather systems (Minobe et al. 2008; Hewitt et al. 2017). Changes due to greenhouse gas forcing in the surface heat fluxes and the meridional overturning cells are intimately related to ocean heat uptake, an issue of enormous societal importance and intensive study (Gregory et al. 2016; Fox-Kemper et al. 2021).

The dynamics of the time-mean meridional overturning circulations (MOCs) are complicated by many factors. For example, the circulations in the three main ocean basins (Atlantic, Indian, and Pacific) are significantly different and interact through the Southern Ocean and Indonesian Throughflow; there are upper, middle, and lower MOC cells; some of these cells interact with the gyre circulations (see section 2c); salinity variations play a major role in the middle and lower cells with the density of water at very high latitudes more dependent on its salinity than its temperature (Huang 2010; Talley et al. 2011; Ferreira et al. 2018; Nilsson et al. 2021); analysis of the energetics of MOCs suggests that wind forcing plays a more important role than internal mixing in driving MOCs (Vallis 2017) but some aspects of the energetics are quite subtle (Gnanadesikan et al. 2005); and there is evidence that mesoscale motions, particularly in the Southern Ocean, play an important role in determining the strength of the middepth cells at least in some model configurations (Abernathey et al. 2011; Munday et al. 2013; Gent 2016).

Dynamically based conceptual models of time-mean MOCs, such as those of Gnanadesikan (1999) and Nikurashin and Vallis (2011), have nonetheless been developed. Johnson et al. (2019) provide a recent survey of the understanding that has been gleaned from conceptual models of MOCs over the last decade. General circulation models (GCMs) are so complex that it is highly desirable to base their interpretation on diagnostics that can be related to such conceptual models.

Denotes content that is immediately available upon publication as open access.

Corresponding author: Michael J. Bell, mike.bell@metoffice.gov.uk

DOI: 10.1175/JPO-D-22-0073.1

This can be useful even if the assumptions on which these conceptual models are based are not entirely valid, providing the departures from the assumptions are quantified and the impact of these departures assessed.

Fields of tracer tendencies driven by the various GCM processes, including the net surface heat fluxes (NSHFs), vertical mixing, advection etc. are powerful diagnostic tools that illuminate how the NSHFs and MOCs in the model relate to the conceptual models. Important analyses of tracer trends in (ϕ, z) space (where ϕ is latitude and z is height) have been provided by Exarchou et al. (2015), Griffies et al. (2015), Kuhlbrodt et al. (2015), Dias et al. (2020), and Saenko et al. (2021). Much of that work focuses on global budgets (as a function of z only), but Griffies et al. (2015) and Dias et al. (2020) in particular also assess spatial patterns of the terms. The theory and literature on the diagnosis of water mass transformations following the ideas of Walin (1982), where the focus is on isothermal (or isohaline or isopycnal) layers, has recently been reviewed by Groeskamp et al. (2019). The analysis of Nurser et al. (1999) is particularly relevant to our discussion as it draws attention first to the relationship between Ekman upwelling velocity and water mass transformation rates in regions where the ocean is absorbing heat and second to the question of whether vertical mixing is dominated by that related to the surface mixed layer (i.e., inside or just outside the mixed layer) or that lower down in the ocean interior. The latter is also addressed for the Southern Ocean by Tamsitt et al. (2018). The surface streamfunction approach of Marsh (2000) and Grist et al. (2014) also has similarities to our approach. Investigations of the energetics of the overturning provide a valuable complementary perspective (von Storch et al. 2012; Zemskova et al. 2015).

The paper has two main aims. The first is to propose interpretations of the NSHFs generated by the Hadley Centre Global Environment Model 3 (HadGEM3) atmosphere–ocean coupled GCM. Our interpretations stem from the dynamically based conceptual models of the MOC derived in Schloesser et al. (2012) and Bell (2015b,a). The interpretations are based on ideas extracted from calculations using layered models that satisfy planetary geostrophic dynamics and are similar to those used to study the ventilated thermocline (Luyten et al. 1983). Two of the most important assumptions made in the ventilated thermocline theory and our interpretations are that water mass transformations occur near the surface and that following the time-mean motion, tracers are mainly changed by these near-surface transformations. These assumptions are very different from those of the abyssal recipes of Munk and Wunsch (1998) in which vertical upwelling is assumed to be balanced by vertical diffusion between 1000- and 4000-m depth. The second main aim is to investigate the validity of these assumptions using tracer trend diagnostics from the GCM.

Section 2a describes the datasets we use. Section 2b then assesses the NSHFs in the HadGEM3 coupled climate models by comparing them with the DEEP-C (Diagnosing Earth's Energy Pathways in the Climate System) estimates of the NSHFs (Liu and Allan 2022). Section 2c presents our interpretation of these NSHFs and the associated MOCs.

Section 3 investigates diagnostics of the terms in the prognostic equations for potential temperature and salinity. Section 3a describes these tracer trend diagnostics. Section 3b investigates the contributions from NSHFs and vertical diffusion with a focus on the latter in a "near-surface" layer. Section 3c considers the contributions from advection and isopycnal diffusion in balancing contributions from other terms. Sections 3d and 3e are somewhat peripheral to the main aims of the paper but are relevant to two important topical issues. Section 3d considers the contributions to heat and salinity tendencies by tracer class summed over all latitudes and basins. Section 3e considers the contributions to the heat content summed over tracer classes within broad latitude bands and investigates the sources of the heat lost in the North Atlantic.

Section 4 summarizes our conclusions and briefly discusses potential further work.

2. Net surface heat fluxes

a. *Description of the data*

The HadGEM3-GC3.1 coupled atmosphere–land–ice–ocean model configurations and integrations used in this study are described in Roberts et al. (2019, hereafter R19). Kuhlbrodt et al. (2018) describes the details of the NEMO (Madec et al. 2022) ORCA1 (L) ocean model configuration and Storkey et al. (2018) describes the details for the ORCA025 (M) and ORCA0083 (H) configurations. The letters L, M, and H denote low, medium, and high resolution, the configurations respectively having 1°, 1/4°, and 1/12° zonal grid spacing at the equator. R19 similarly denote their atmosphere–land configurations by the letters L, M, and H, the midlatitude grid spacing being 135, 60, and 25 km, respectively. We use the coupled configurations denoted by LL, MM, and HH, the first letter indicating the atmosphere and the second the ocean configuration. In these configurations very few parameters explicitly depend on the grid resolution of the atmosphere or the ocean model. However, the representation of the ocean mesoscale in the L configuration is largely parameterized while in the M and H configurations it is increasingly represented explicitly (at least at lower latitudes). As described in Storkey et al. (2018) and summarized in Table 1, the representation of eddy-induced fluxes (Gent and McWilliams 1990) is only used in the L configuration and the isopycnal diffusion coefficient is set equal to 1000, 150, and 125 $m^2\ s^{-1}$ in the L, M, and H configurations, respectively. Vertical mixing of tracers is parameterized using a modified form of the Gaspar et al. (1990) TKE scheme, a background vertical eddy diffusivity of $1.2 \times 10^{-5}\ m^2\ s^{-1}$, and the Simmons et al. (2004) scheme for vertical mixing by the dissipation of internal tides (see Storkey et al. 2018 for details).

We use the integrations referred to by R19 as control-1950 and hist-1950. Control-1950 uses forcing datasets (for solar heating, greenhouse gases, aerosols, etc.) representing conditions in the 1950s while hist-1950, uses forcing representing historic conditions from 1950 to 2014. Both of these integrations start after a 30-yr spinup using the 1950s forcing. The initial conditions for the spinup are the January 1950–54 mean

TABLE 1. The resolutions and resolution dependent parameterizations of the HadGEM3-GC3.1 configurations.

	LL	MM	HH
Ocean model zonal grid spacing at equator (°)	1	1/4	1/12
Atmosphere model grid spacing at midlatitudes (km)	135	60	25
Isopycnal diffusion coefficient ($m^2\ s^{-1}$)	1000	150	125
GM parameterization of eddy-induced velocities	Held and Larichev (1996)	None	None
Lateral viscosity	Laplacian: $2 \times 10^4\ m^2\ s^{-1}$	Biharmonic: $-1.5 \times 10^{11}\ m^4\ s^{-1}$	Biharmonic: $-1.25 \times 10^{10}\ m^4\ s^{-1}$

EN4 ocean analysis (Good et al. 2013) and the ERA-20C atmosphere analysis in January 1950 (see R19 for more detail).

The DEEP-C version 5 NSHF product (Liu and Allan 2022) used in this study is derived from reconstructions of the net radiation at the top of the atmosphere calculated using measurements from the CERES (Clouds and the Earth's Radiant Energy System) satellite and energy flux divergences calculated from the ERA5 (fifth-generation ECMWF ReAnalysis) atmospheric reanalyses using techniques described in Liu et al. (2015) and Mayer et al. (2017). Liu et al. (2017) provide evaluations of the accuracy of these fluxes, and Hyder et al. (2018, their supplementary Fig. 1) show that these DEEP-C estimates are much more reliable than previous products.

Diagnostics for the Pacific, Atlantic, and Indian Oceans have been calculated using the "standard" basin masks for each configuration. These masks have been extended into the Southern Ocean taking the boundaries between the basins to lie at 25°E, 135°E, and 70°W.

b. *Comparison of model and DEEP-C net surface heat fluxes*

Figure 1 compares annual mean NSHFs for the period 2000–09 calculated using an 8-member ensemble of LL hist-1950 HadGEM3-GC3.1 integrations and the DEEP-C product. The patterns and magnitudes of the two sets of NSHFs are generally in good agreement. The strong net surface heating regions agree well in the eastern equatorial Pacific; the equatorial Atlantic; the South Atlantic and southwestern Indian Ocean (between 45° and 60°S); and on the eastern boundaries of the Atlantic and Pacific, particularly in the Northern Hemisphere to the west of Africa and the American continent. The strong net surface cooling regions agree well in the North Atlantic and south of 60°S, and in the western boundary current extensions of the Gulf Stream, Kuroshio, East Australian Current, Brazil Current, and the Agulhas Retroflection. There are also several other regions of weaker surface fluxes where the agreement is qualitatively good and the large region of surface heat loss in the eastern Indian Ocean between the equator and 30°S also agrees well.

Figure 2a shows the difference between the fluxes presented in Fig. 1. Figures 2b and 2c present the corresponding differences for 3- and 4-member ensembles of the MM and HH hist-1950 integrations, respectively. The largest differences between these three plots are in the northwest Atlantic where the positive difference progressively reduces as the model resolution improves. This reflects an improvement in the path of the Gulf Stream to the east of the Grand Banks which corrects a notorious cold bias in the LL model (Scaife et al. 2011) and most other climate models of similar or only slightly better resolution (Smith et al. 2000). The differences in the Agulhas retroflection and Kuroshio regions for the HH simulation are also smaller than those for the other simulations. In most other regions the differences between the NSHFs are relatively independent of model resolution. There are for example similar large differences in the western Indian

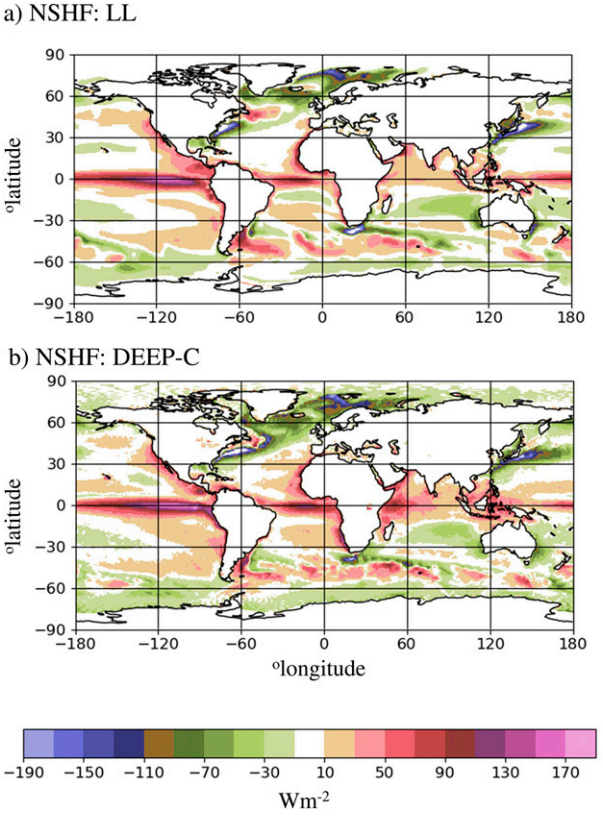

FIG. 1. Annual mean NSHF (W m^{-2}) for the period 2000–09 calculated (a) from an ensemble of eight HadGEM3-GC3.1 N96 ORCA1 hist-1950 simulations and (b) using the DEEP-C methodology.

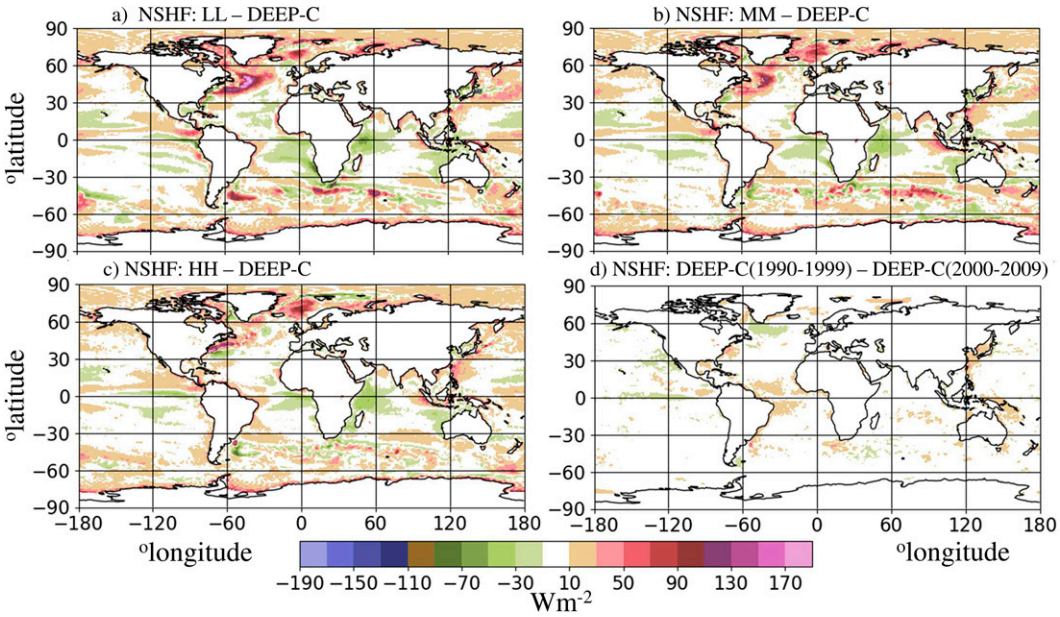

FIG. 2. Annual mean NSHF for the period 2000–09 from hist-1950 coupled climate model integrations minus that calculated using the DEEP-C methodology for the same period using: (a) an 8-member LL ensemble, (b) a 4-member MM ensemble, and (c) a 3-member HH ensemble. (d) NSHFs calculated by DEEP-C: 1990–99 minus 2000–09.

ocean near the equator. This may be because of inaccuracies in the DEEP-C product or resolution independent inaccuracies in the atmosphere model (none of the configurations resolves convection cells). Figure 2d shows the difference between the DEEP-C fluxes for 1990–99 and 2000–09. These differences and the interdecadal variations in the model heat fluxes (not shown) are smaller than the differences shown in Figs. 2a–c.

Figures 3a–d display the net heat input by latitude band calculated from DEEP-C v5 and the LL, MM, and HH control integrations for the decade 2000–09. There is generally good qualitative and quantitative agreement between all four products. The Pacific dominates the heat input in the equatorial band between 15°S and 15°N in all the products, being about twice as large as the heat input in the Atlantic and Indian Oceans combined.

c. *Linking net surface heat fluxes to MOCs*

Gnanadesikan (1999) proposed a conceptual model of the middle MOC cell which was motivated by the idea that this cell "connects" the region of heat loss in the North Atlantic to that of heat gain in the Southern Ocean. Bell (2015a) aimed to explain why, in agreement with the NSHF products available at the time, this heat gain in the Southern Ocean is focused on the South Atlantic and southwestern Indian Ocean. His conceptual model was based on somewhat complicated calculations using the planetary geostrophic equations which aimed to apply the techniques developed with great success by Luyten et al. (1983) for the ventilated thermocline to describe MOCs. These calculations cannot be used directly to diagnose GCM output because they are limited to models with small numbers of vertical layers and relatively simple forcing scenarios. Some key ideas can nonetheless be distilled from these calculations and used to interpret the GCM outputs.

The main ideas, which are illustrated schematically in Fig. 4 and described in more detail below, are as follows:

1) The depths of isopycnals are almost independent of latitude along eastern boundaries.
2) In regions where there is a time-mean net surface heat flux into the ocean (e.g., in the eastern equatorial basins and Southern Ocean), Ekman upwelling supplies the flux of cold water that balances the surface heating.
3) The warm water that is formed near the equator will accumulate on the western side of the basins until it is entrained/advected poleward by the western boundary currents and loses its heat to the atmosphere.
4) The thermocline on the eastern boundary of the Atlantic will deepen until the poleward flow driven by thermal wind shear results in surface heat loss in the North Atlantic which is in balance with heat uptake driven by Ekman upwelling elsewhere (see idea 2 above).
5) The surface and deep western boundary currents are able to close the circulations generated by the winds and water mass transformations in the geostrophic interior.

Figure 5 illustrates the 3D structure of the potential temperature field associated with the surface fluxes. For simplicity of presentation, in this figure the ocean is taken to consist of one basin with due north–south boundaries that spans the equator. The vertical cross sections lie along the equator (bottom right), across the path of a separated western boundary current (WBC) (top left), just north of the Drake Passage (bottom left), and in the northeast Atlantic (top right). The

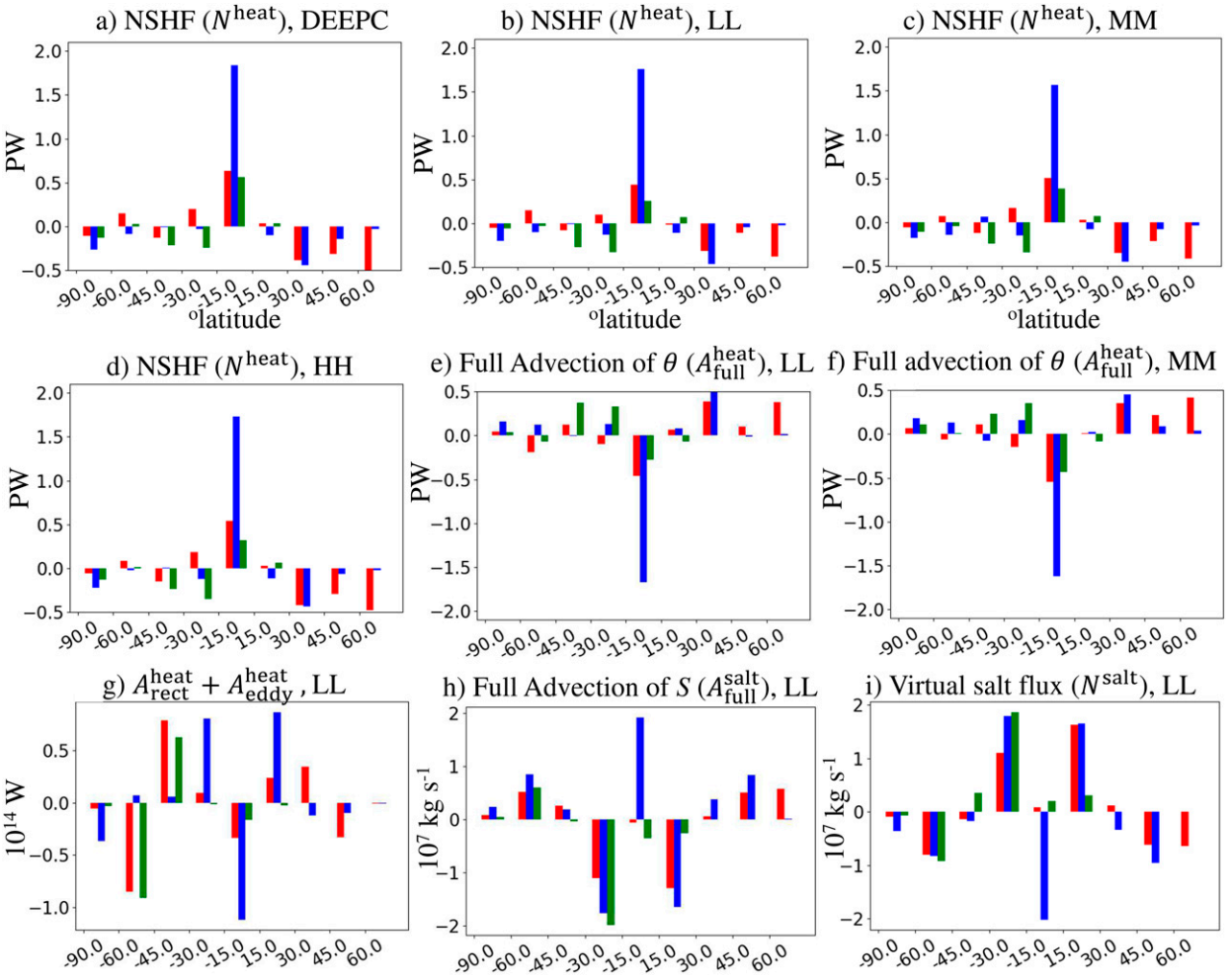

FIG. 3. Calculations by latitude band and ocean basin (red Atlantic, blue Pacific, and green Indian Ocean) of NSHF (PW) using (a) DEEP-C and (b)–(d) the LL, MM, and HH preindustrial control simulations, respectively. (e)–(i) Additional terms defined in section 3a and Table 1. All figures use data for the period 2000–09.

figure emphasizes the water mass transformations (purple arrows) related to Ekman upwelling and surface heating, or to poleward advection and surface cooling. Some aspects of the structure of the potential temperature field are discussed in more detail below.

The first idea, that the depths of neutral density surfaces should be relatively independent of latitude along the eastern boundaries of each of the major ocean basins, is based on the condition of no normal flow at the boundary and our knowledge of boundary waves (Marshall and Johnson 2013). There is evidence that this is a good approximation in GCMs, at least within about 40°–50° of the equator, but the details deserve separate publication. Hughes et al. (2018) present an extensive study of the related issue of bottom pressure variations along the ocean boundaries. Where the ocean potential density is primarily determined by the potential temperature (again within about 40°–50° of the equator) this implies that the near-surface temperature will be relatively independent of latitude compared with the atmospheric surface temperature. Note that within all the sections in Fig. 5 that contain an eastern boundary (all of them other than the one on the top left) the depths of the isotherms on the eastern boundary are the same (i.e., independent of latitude).

The second idea is that in regions where there is a sustained (i.e., time-mean) NSHF into the ocean, there must be a compensating provision of cold water to the surface and that this is most likely to be supplied by Ekman upwelling of cold water from below (or equatorward transport by Ekman transports). Along the equatorial Pacific (and Atlantic) it is well known that prevailing winds from the east cause the thermocline that is deep in the west of the basin to shoal in the east, as shown in the bottom-right section of Fig. 5. The upwelling at the equator is very strong because there is a strong poleward Ekman transport on both sides of the equator at about 3°–5° from the equator. Where relatively cold water is upwelling and being converted into warmer water by the surface fluxes, the rate of water mass transformation must be equal to the upwelling velocity (Nurser et al. 1999; Bell 2015a). The

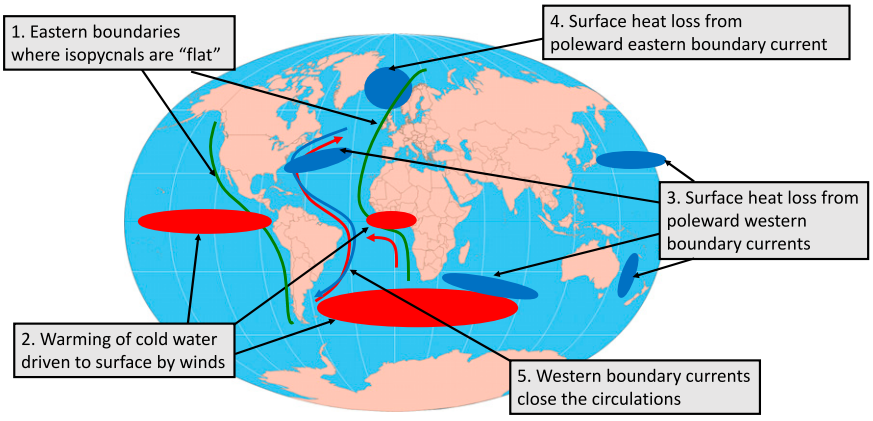

FIG. 4. Schematic outlining how the main geographical patterns of the NSHF are interpreted as arising from basic dynamical processes.

location of the region of surface heating in the South Atlantic and southwest Indian Ocean (see Fig. 4 and also Fig. 1) relates to the westward outcropping of water in a subpolar supergyre, treating the region north and west of Drake Passage as a subpolar gyre that extends right around the globe (Stommel 1957; Bell 2015b; Marshall et al. 2016; Tamsitt et al. 2016). This westward outcropping is illustrated in the bottom-left section of Fig. 5. The regions of surface heating on the west coasts of Africa and North America mentioned earlier are related to coastal Ekman upwelling.

The third idea (Gnanadesikan 1999) is that, in a steady state, the total rate at which a water mass is being formed must be the same as the rate at which it is being destroyed (i.e., converted into other water masses). The warm water formed by Ekman upwelling and net surface heating in the eastern equatorial Pacific (and Atlantic) accumulates on the western side of the basin and is entrained in the western boundary currents and exported poleward as a tongue of warm water as shown in the top-left section in Fig. 5. These currents that are relatively warm compared to the atmosphere are then expected to provide a significant source of heat (and moisture) to the atmosphere.

The fourth idea, discussed in detail in Bell (2015a), is that the poleward flow into the northeast Atlantic is due to an eastern boundary current (the Norwegian Coastal Current) associated with the relatively warm water at high latitudes on the eastern boundary. By neglecting the surface wind stresses in the North Atlantic, a rather general solution to the nonlinear planetary geostrophic equations can be obtained and the area-integrated net surface heat loss related to the depths of

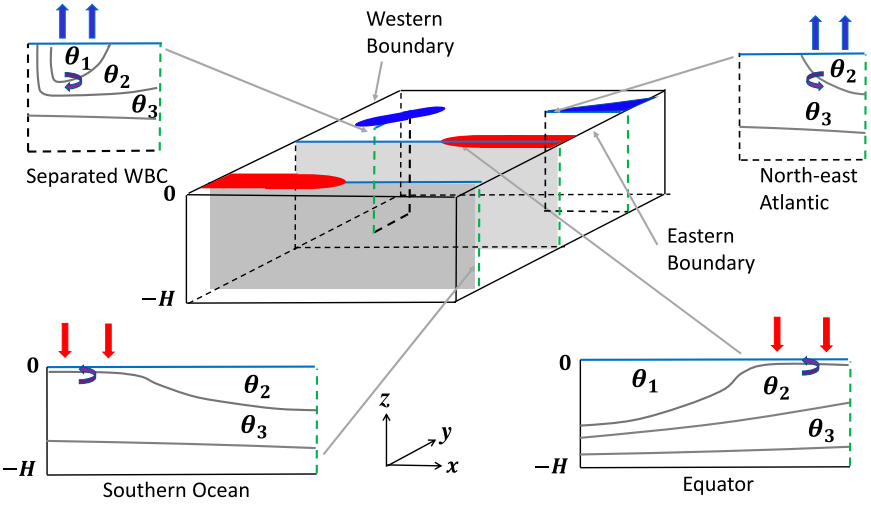

FIG. 5. Schematic depicting vertical cross sections through an ocean with three active layers of water of different potential temperatures (from θ_1 to θ_3). Net surface heating and cooling (thick red and blue arrows) transform cooler to warmer water and warmer to cooler water, respectively (purple arrows). The regions of heat uptake are associated with Ekman upwelling and the regions of heat loss with poleward advection of the upper layer. The ocean has one square-shaped basin with due north–south eastern and western boundaries solely to simplify its presentation.

the isotherms on the eastern boundary. It is suggested that the lack of a similar heat loss in the Pacific is associated with the fresh surface salinities in the North Pacific (Huang 2010). The isotherm slope that gives rise to the thermal wind shear and the poleward surface flow is shown in the upper-right section of Fig. 5.

The final idea, that the western boundary currents are turbulent and passive, i.e., able to adjust to a geostrophic interior, is commonly used in conceptual models. A final important point about Fig. 5 is that the 3D circulations induced by these water mass transformations, being influenced by the gyre circulations, their boundary currents, and seasonal variations, can be expected to have complex (chaotic) Lagrangian trajectories, the mixing being further enhanced by mesoscale structures in frontal regions (Iudicone et al. 2008b; Tamsitt et al. 2018; van Sebille et al. 2018). Steady-state 2D representations of MOCs cannot represent such complex trajectories.

Although there is nothing particularly new or surprising in the ideas described above, their combination in this form seems to be somewhat novel and should be regarded with caution. In particular it is not yet clear to what extent these ideas are valid or helpful for assessing GCMs. The following section begins to explore these issues.

3. Tracer trend diagnostics

The data used in this section are monthly means from control integrations for the 10-yr period 2000–09. The control (rather than the historical) integrations are used because, after 50 years of integration, they should be drifting relatively slowly and the tracer trend budgets should be closer to equilibrium than those of the historical simulations.

a. Methods used to calculate tracer trend diagnostics

The NEMO code used in this study is couched in s coordinates in which cell thicknesses are allowed to change with time. Our integrations used z^* coordinates (Roullet and Madec 2000; Adcroft and Campin 2004), a particular choice of s coordinates. In s coordinates a model tracer cell is referred to by its pseudozonal index i, pseudomeridional index j, and depth index k. Its vertical thickness e_3 may depend on all these indices and vary in time, $e_3(i, j, k, t)$, while its pseudozonal width $e_1(i, j)$ and pseudomeridional width $e_2(i, j)$ do not depend on k or t. The volume-integrated tendency T_{ijk} for a tracer τ is given (see section A.2 of Madec et al. 2022) by

$$T_{ijk} \equiv \frac{\partial(e_1 e_2 e_3 \tau)}{\partial t} = A_{ijk} + (D_v)_{ijk} + (D_{\text{iso}})_{ijk} + N_{ijk}, \qquad (1)$$

where advection

$$A_{ijk} = -\frac{\partial(e_2 e_3 u\tau)}{\partial i} - \frac{\partial(e_1 e_3 v\tau)}{\partial j} - \frac{\partial(e_1 e_2 \omega\tau)}{\partial k}, \qquad (2)$$

and $(D_v)_{ijk}$, $(D_{\text{iso}})_{ijk}$, and N_{ijk} represent the tracer gain by vertical diffusion, isopycnal diffusion, and net surface fluxes, respectively, while u and v represent the i and j velocities and ω is the upward vertical velocity with respect to the s-coordinate surface (which is itself moving).

For the Coupled Model Intercomparison Project (CMIP), monthly mean 3D fields of these individual terms in the prognostic equations for potential temperature θ and salinity S were generated by accumulating them "on the fly" each time step. Each cell-integrated term in (1) for θ is multiplied by $c_p\rho_0$ (where c_p is the specific heat capacity per unit mass and ρ_0 the mean density of the Boussinesq ocean) to output cell-integrated rates of heat increase in watts. Similarly, we multiply each salinity term by $0.001\rho_0$ to give cell-integrated rates of salt mass increase, with units of kilograms per second (kg s^{-1}). We have verified that the four processes on the rhs of (1) sum to the local rate of change of cell-integrated heat and salt content with good accuracy at each grid cell.

To bin the heat content change into potential temperature classes, we divide the interval from −6° to 44°C into 200 θ bins of width 0.25 K, and assign the cell-integrated value of each term in each cell to the two nearest θ classes whose central values bracket the cell's monthly-mean temperature (cf. Lee et al. 2002). The fraction w donated to one of these classes varies linearly from 1, when the gridcell θ is the same as the central value of the class, to 0 when it equals the central value of the other class. The fraction donated to the other class is given by $1 - w$. The same approach is used to allocate latitude to 180 latitude bins each of 1° width. We bin the salt content change similarly, but into 200 salinity classes of width 0.05 psu and the same latitude bins as the heat terms. Our analysis focuses on these monthly mean heat and salt content trend diagnostics calculated separately for the Atlantic, Indian, and Pacific Ocean basins as functions of ϕ and θ (or S).

Clearly it would be preferable to assign each of the terms to their classes on every time step (as in Hieronymus and Nycander 2013; Holmes et al. 2019a, 2021), rather than assign monthly mean terms using monthly mean values of θ. Code to achieve this is not currently available in the NEMO system, however, and we follow Jackson et al. (2020) and Saenko et al. (2021) in using the monthly mean data that are readily available. Daily mean surface fluxes and surface values of θ and S are available and have been found to generate results for surface fluxes that are quite similar to those generated using monthly mean data.

Table 2 summarizes the terms and the names and symbols we use for them. The binned terms for the heat and salt content tendencies will be denoted by capital letter symbols without the ijk subscript. These binned terms should satisfy

$$T = A_{\text{full}} + N + D_{\text{iso}} + D_v. \qquad (3)$$

We have also attempted to calculate the contribution to the rates of change of heat and salt contents from the time-mean advection of time-mean fields. For any field q, let us denote the monthly mean of q by $\overline{q}$, deviations of q from $\overline{q}$ by $q' = q - \overline{q}$, and the values of τ linearly averaged onto the u, v and w faces of the tracer cell on the C-grid by τ_u, τ_v, and τ_w. We have used the three components of $(\overline{u\tau_u}, \overline{v\tau_v}, \overline{w\tau_w})$, that

TABLE 2. Description of the terms in the tracer prognostic equations.

Symbol	Name	More detailed description
A	Advection	
A_{eddy}	Eddy-induced advection	Eddy induced advection (GM flux)
A_{full}	Full advection	Full advection including advection by eddy induced velocity
A_{mean}	Mean advection	Advection of the time-mean field by the time-mean flow
A_{rect}	Rectifying advection	An estimate of the advection of the time-varying field by the time varying flow
D	Diffusion	
D_{iso}	Isopycnal diffusion	
D_v	Vertical diffusion	Vertical diffusion (including mixing by convection and mixing resulting from tides)
$D_{v,\text{ns}}$	Near-surface vertical diffusion	Vertical diffusion restricted to near to the surface [see (12)]
N	Net surface flux	
N^{heat}	NSHF	Net surface heat flux
$N^{\text{heat}}_{\text{srf}}$	Surface-assigned NSHF	Net surface heat flux with the solar flux all artificially assigned to (absorbed at) the surface
N^{salt}	Virtual salt flux	Net virtual salt flux [see (7)]
N^{dens}	Surface density flux	Net surface potential density flux [see (8)]
$N + D_v$	Vertically mixed net surface flux	Sum of the net surface flux and the vertical diffusion
$N^{\text{heat}} + D_v^{\text{heat}}$	Vertically mixed NSHF	Sum of the NSHF and the vertical diffusion
T	Total tendency	Rate of change of tracer calculated from the differences between the start and end of the month

are calculated by the model on the fly, together with $(\overline{u}, \overline{v}, \overline{w})$ and $\overline{\tau}$ to calculate the rectifying advection A_{rect}, defined as the divergence of $(\overline{u'\tau'_u}, \overline{v'\tau'_v}, \overline{w'\tau'_w})$. The eddy-induced advection A_{eddy} is calculated similarly from the divergence of $(\overline{u}_e\,\overline{\tau}_u, \overline{v}_e\,\overline{\tau}_v, \overline{w}_e\,\overline{\tau}_w)$, where $\overline{u}_e$, $\overline{v}_e$, and $\overline{w}_e$ are the eddy-induced velocities at the tracer cell faces calculated using the Gent–McWilliams scheme (Gent and McWilliams 1990). These calculations of A_{rect} and A_{eddy} are only estimates because they use values of the tracer at the cell faces linearly interpolated from the grid centers rather than the higher-order and flux-limited values used by the advection scheme within the model. The calculations of these terms for the heat content appear to be reliable but A_{eddy} for salinity is noisy and we have elected not to use it. Given our definitions of A_{full}, A_{rect}, and A_{eddy}, our estimate of the tendency due to the advection of the monthly mean τ by the monthly mean flow is

$$A_{\text{mean}} = A_{\text{full}} - A_{\text{eddy}} - A_{\text{rect}}. \tag{4}$$

The NEMO code used in the integrations has a fully nonlinear free surface in which evaporation and precipitation provide surface mass fluxes of freshwater, expressed as a flux through the top of the uppermost grid cell. No virtual surface source or sink of salt, such as is necessary in models with a rigid lid, is explicitly imposed in the model. There is therefore no explicit N^{salt} term, and the advection term A_{ij1} of (2) effects the surface salinity changes associated with the surface freshwater flux through the compensating advection of saltier water through the base of the surface grid cell. However, for our diagnostics, we wish to separate out the effect of interior advection from these surface mass fluxes and we find it convenient to decompose a net freshwater outward flux (e.g., Nurser and Griffies 2019) into (i) an outward flux of the same mass (converted to a volume flux for the Boussinesq NEMO model):

$$e_V = \rho_0^{-1}(e - p - r_I), \tag{5}$$

where $e - p - r_I$ is the usual upward mass flux associated with evaporation minus precipitation minus river input, but with salinity equal to the surface salinity; this gives an advective salt *sink* equal to $0.001 S \rho_0 e_V$ and (ii) a massless *source* of salt balanced by an outward flux of freshwater:

$$e_S = 0.001\, S \rho_0 e_V. \tag{6}$$

This massless salt source recovers the virtual surface source used in rigid-lid models. It is area integrated over the surface grid cell $ij1$ to give

$$(N^{\text{salt}})_{ij1} = e_1 e_2 e_S, \tag{7}$$

which has the correct units (kg s^{-1}) and may then be binned in salinity like the other terms to give the binned N^{salt} field. Of course, for (3) (with $N = N^{\text{salt}}$) to remain valid it is now necessary to subtract this N^{salt} from the advection A_{full}; this physically represents that the advection term now "sees" a surface inflow of water (5) with salinity S rather than freshwater (salinity zero).

We have also calculated the monthly mean potential density ρ, thermal expansion coefficient α, and saline contraction coefficient β at each grid point using θ, S, and $z = 0$ with the model's equation of state (EOS80) as implemented by Roquet et al. (2015). Each of the monthly mean density terms X^{dens}, where X stands for one of the letters in Table 2, is then calculated from the corresponding heat and salt terms, X^{heat} and X^{salt}, using

$$X^{\text{dens}} = \rho_0\left(-\frac{\alpha X^{\text{heat}}}{\rho_0 c_p} + \beta\frac{X^{\text{salt}}}{0.001\rho_0}\right). \tag{8}$$

These values have been assigned to 200 classes of width 0.1 kg m^{-3}.

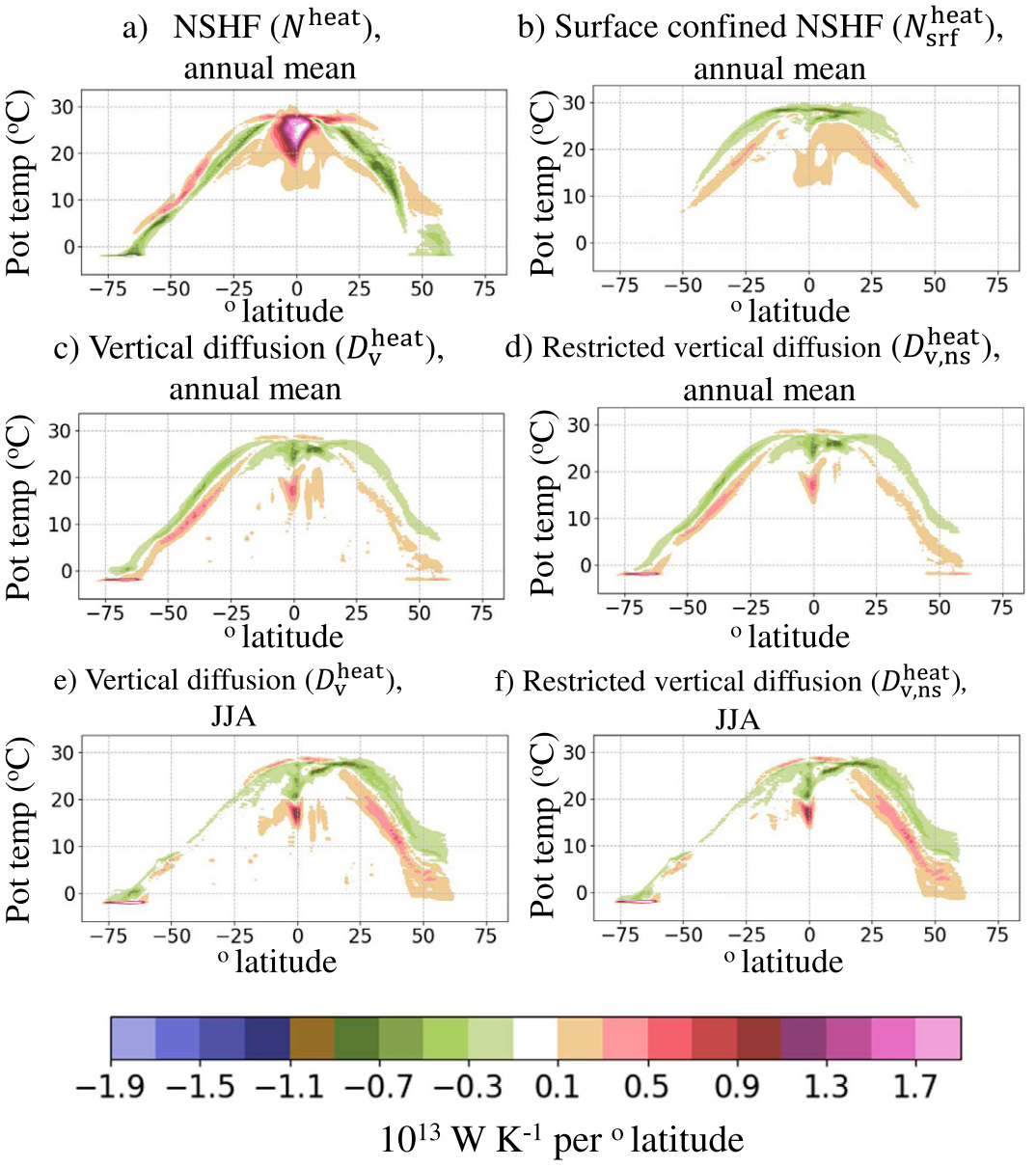

FIG. 6. (a)–(f) Mean net heat flux divergences, as defined in Table 2, for the Pacific Ocean from the LL control integration over the period 2000–09 as a function of latitude and potential temperature class. The solar penetration in (b) is the NSHF minus the surface-assigned NSHF ($N^{heat} - N^{heat}_{srf}$). The near-surface vertical diffusion in (d) and (f) is limited [Eq. (12)] to 1.2 times the monthly maximum MLD or 100 m of the surface. Panels (e) and (f) are means for the boreal summer (JJA). Saturated values are colored white.

In Boussinesq water-mass transformation theory (e.g., Nurser et al. 1999; Groeskamp et al. 2019), the binned heat inputs are generally divided by the bin width to give volume fluxes F_X across the isotherms, according to

$$F_X = \frac{X^{heat}}{\rho_0 c_p \Delta\theta}. \tag{9}$$

Given that the heat inputs are binned also in latitude, (9) would give the volume flux across the isotherm within the latitude bin. Here, however, we choose to simply bin the heat, salt, and mass fluxes because we are concentrating on the heating and freshening processes.

We use two measures for how well one field F_i represents a second field G_i. The first is a normalized mean square error:

$$\text{NMSE} = \sum_i \frac{(F_i - G_i)^2}{S(F)S(G)}, \; S(F) \equiv \sqrt{\sum_i F_i^2}. \tag{10}$$

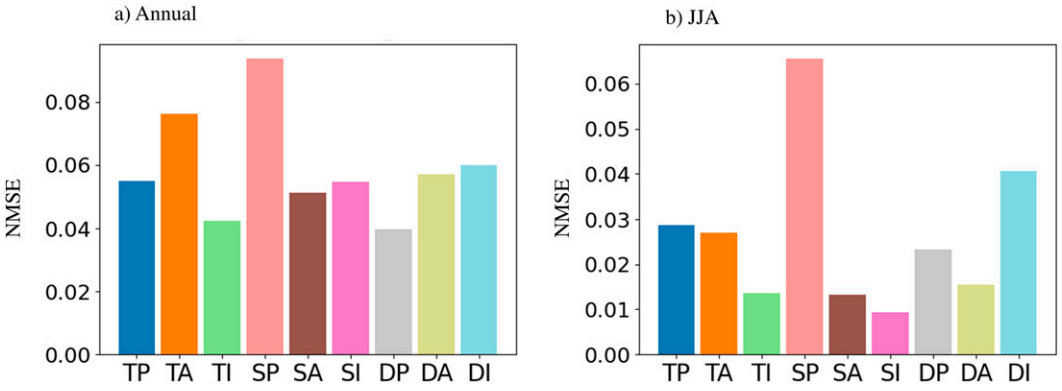

FIG. 7. The normalized mean square error (NMSE) in representing D_v by $D_{v,\mathrm{ns}}$ calculated using (12) with $a = 1.2$ and $d_0 = 100$ m for (a) annual means and (b) boreal summer (JJA). The first letter, T, S, or D, on the abscissa indicates potential temperature, salinity, or density, respectively. The second letter, P, A, or I, indicates the Pacific, Atlantic, or Indian Ocean basin, respectively.

The smaller the value of the NMSE the better F reproduces G. The second measure is the pattern correlation coefficient:

$$\mathrm{PCC} = \sum_i \frac{F_i G_i}{S(F)S(G)}. \tag{11}$$

b. *How much of the vertical mixing is confined to near-surface layers?*

Figure 6 presents terms for the rate of change of heat content in the Pacific Ocean. Figure 6a shows the annual mean NSHF term N^{heat}, which is the net of the heat input by solar radiation, taking account of the depth of penetration, and the heat lost from the surface due to turbulent fluxes (latent and sensible heat fluxes) and longwave radiation. Figure 6b shows the annual mean $N^{\mathrm{heat}} - N^{\mathrm{heat}}_{\mathrm{srf}}$, where $N^{\mathrm{heat}}_{\mathrm{srf}}$ is the net heat input taking all the solar radiation to be absorbed at the surface. One sees that the penetration of the solar flux makes an appreciable difference to the temperature distribution of the "surface" fluxes. This important point has been noted previously by Nurser et al. (1999), Iudicone et al. (2008a), Hieronymus and Nycander (2013), and Groeskamp and Iudicone (2018).

The redistribution of heat by vertical diffusion D^{heat}_v in the annual mean, shown in Fig. 6c, is also significant. This redistribution has a very strong seasonal variation, except possibly near the equator, with D^{heat}_v being strongest in midlatitudes during summer months (not shown). The large seasonal variation suggests that the dominant contribution to the Vertical diffusion may be associated with mixing within or just below the surface mixed layer. We have explored this hypothesis by calculating additional diagnostics $D^{\mathrm{heat}}_{v,\mathrm{ns}}$ in the same way as D^{heat}_v except that the contributions are restricted to depths less than $d_{\max}$ where

$$d_{\max}(\lambda, \phi, m) = \max[a \times \mathrm{MLD}_{\max}(\lambda, \phi, m), d_0]. \tag{12}$$

Here λ is longitude, m is month, $\mathrm{MLD}_{\max}(\lambda, \phi, m)$ is the maximum mixed layer depth in the month (as a function of geographical location) calculated following Kara et al. (2000), a is a factor slightly larger than 1 and d_0 is a constant value. One would expect a value of a of order 1.2 to be sufficient to capture vertical mixing confined to the mixed layer and entrainment into it. Comparison of $D^{\mathrm{heat}}_{v,\mathrm{ns}}$ calculated using $a = 1.5$ and $d_0 = 0$ with the full D^{heat}_v (not shown) reveals that not all of the vertical mixing is associated with mixed layer processes. Figure 6 displays D^{heat}_v (left) and $D^{\mathrm{heat}}_{v,\mathrm{ns}}$ (right) calculated using $a = 1.2$ and $d_0 = 100$ m with annual mean and boreal summer data (in the middle and lower panels, respectively). One sees that in both cases $D^{\mathrm{heat}}_{v,\mathrm{ns}}$ using this combination reproduces D^{heat}_v very closely. We conclude that although not all the vertical diffusion is associated with mixed layer processes, the vast majority of it is either associated with mixed layer processes or occurs within 100 m of the surface.

Motivated by this result, we will define the near-surface layer to be the layer within a depth $d_{\max}$ of the surface given by (12) with $a = 1.2$ and $d_0 = 100$ m. Figure 7 shows that the result holds in the other ocean basins and for salinity and density as well as heat content. It displays the normalized mean squared differences, (10), between $D_{v,\mathrm{ns}}$ and D_v calculated for each of these terms using annual means (Fig. 7a) and the boreal summer months (JJA; Fig. 7b). Similarly small values of NMSE are obtained for the three other seasons.

c. *How well correlated are mean advection and near-surface flux inputs?*

Because the total rate of change T is small (it would appear almost completely white using the contour intervals in Fig. 6), (3) implies that many sums of terms (such as $A_{\mathrm{full}} + N$ and $D_{\mathrm{iso}} + D_v$) are almost perfectly anticorrelated for all of the tracers. Rather than exploring arbitrary combinations, this subsection deliberately compares contributions from $N + D_v$, the net surface flux taking into account vertical mixing in the near-surface layer, with various estimates of the advection and isopycnal diffusion terms. Our focus will be on the patterns in (ϕ, class) space of the advection by the mean flow, A_{mean} [see (4)], because the interpretation of the previous section assumes that these terms are dominant, in which case they should be strongly anticorrelated with $N + D_v$.

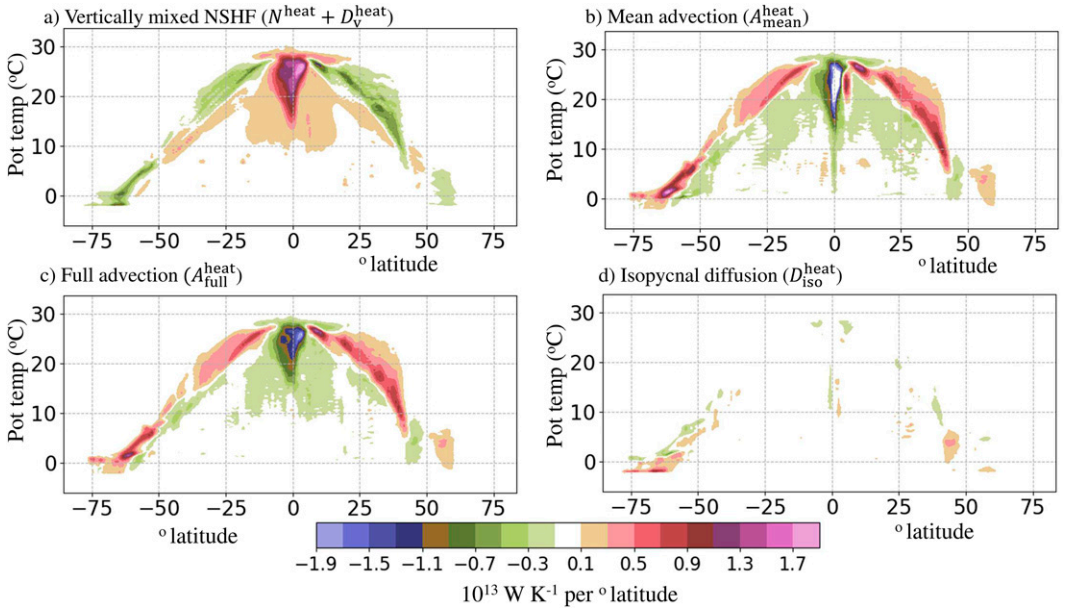

FIG. 8. Mean net heat flux terms for the Pacific from the LL control integration over 2000–09.

We present results for heat, salt, and density tendencies in the Pacific, Atlantic, and Indian Ocean basins. As this is a lot of information, we suggest that on first reading after Fig. 8 the reader bypasses Figs. 9–12 and proceeds directly to Fig. 13, which summarizes the statistics of the correlations.

Starting with heat term contributions, Fig. 8 allows one to compare $N^{heat} + D_v^{heat}$ for the Pacific in the LL simulation with A_{mean}^{heat} [calculated from (4)] and D_{iso}^{heat}. It is clear that $N^{heat} + D_v^{heat}$ is very well anticorrelated with A_{full}^{heat}. At high latitudes, particularly in the Southern Hemisphere, D_{iso}^{heat} makes an appreciable but by no means dominant contribution (Gregory 2000). One can see from Figs. 8a, 8c, and 8d that the regions at high latitudes where A_{full}^{heat} and $N^{heat} + D_v^{heat}$ are not well anticorrelated are precisely those where D_{iso}^{heat} is nonnegligible.

In addition to the regions of strong negative values (representing cold advection, or a net influx of colder water) at the equator, A_{mean}^{heat} and A_{full}^{heat} in Fig. 8 have slanting regions of strong positive values (warm advection) which extend from close to the equator to about 40°N and 35°S. We interpret these as being associated with boundary currents advecting warm water poleward. It is evident from figures for A_{rect}^{heat} and A_{eddy}^{heat} for the LL Pacific simulation (not shown) that the contributions from A_{rect}^{heat} are quite important near the equator and small elsewhere, while A_{eddy}^{heat} contributes at high latitudes, particularly in the Southern Hemisphere, and at midlatitudes. Like $N^{heat} + D_v^{heat}$, A_{rect}^{heat} warms the equatorial ocean. It seems very likely that this is associated with tropical instability waves fluxing heat toward the equator (e.g., Bryden and Brady 1989; Graham 2014). The fact that A_{mean}^{heat} is "balanced" by both N^{heat} and $A_{rect}^{heat} + A_{eddy}^{heat}$ on the equator is consistent with the idea that wind-driven Ekman upwelling is driving the uptake of heat from the atmosphere in this region.

Figure 9 presents $N^{heat} + D_v^{heat}$ and A_{mean}^{heat} from the LL integration calculated for the Atlantic (top) and Indian Ocean (bottom). $N^{heat} + D_v^{heat}$ and A_{mean}^{heat} are clearly well anticorrelated in many regions of significant heat gain or loss. The heating by A_{mean}^{heat} in the Atlantic clearly extends much further north (as far as 80°N) than it does in the Pacific (only to 40°N). In the Indian Ocean, relatively little heat is absorbed at the equator and there are two distinct regions where heat is supplied by A_{mean}^{heat} and lost through surface fluxes $N^{heat} + D_v^{heat}$.

Figure 10 presents $A_{rect}^{heat} + A_{eddy}^{heat}$ and D_{iso} for the Atlantic from the LL and MM integrations. D_{iso}^{heat} is nonnegligible over a wider region in the Atlantic than the Pacific, particularly in the Northern Hemisphere. The factor of 6 reduction in the isopycnal diffusion coefficient in MM weakens D_{iso}^{heat} significantly but by a much smaller factor than 6, presumably because tracer gradients on isopycnals steepen (Figs. 10b,d). Despite the fact that $A_{eddy}^{heat} = 0$ in the MM integration, $A_{rect}^{heat} + A_{eddy}^{heat}$ is of comparable importance in the LL and MM integrations, as the stronger eddies that develop in the MM simulation give a larger A_{rect}^{heat}. Note though that away from the equator the patterns of the fields differ considerably.

In salinity space, (ϕ, S), the A_{full}^{salt}, N^{salt}, D_{iso}^{salt}, and D_v^{salt} terms are all of a similar order of magnitude. A_{rect}^{salt} is relatively small except close to the equator and, as mentioned already, A_{eddy}^{salt} is unacceptably noisy at some points in (ϕ, S) space. As it is relatively small compared to the other main terms at other points in (ϕ, S) space, we estimate A_{mean}^{salt} from $A_{full}^{salt} - A_{rect}^{salt}$ neglecting A_{eddy}^{salt}. Figure 11 compares $N^{salt} + D_v^{salt}$, $A_{full}^{salt} - A_{rect}^{salt}$, D_{iso}^{salt} and D_v^{salt} for the Pacific. Even though D_{iso}^{salt} is relatively more important than before, $N^{salt} + D_v^{salt}$ and $A_{full}^{salt} - A_{rect}^{salt}$ are clearly anticorrelated. In all three ocean basins, negative values of D_{iso}^{salt} and D_v^{salt} generally occur for higher salinities than the positive values and the opposite is true for N^{salt} (not shown).

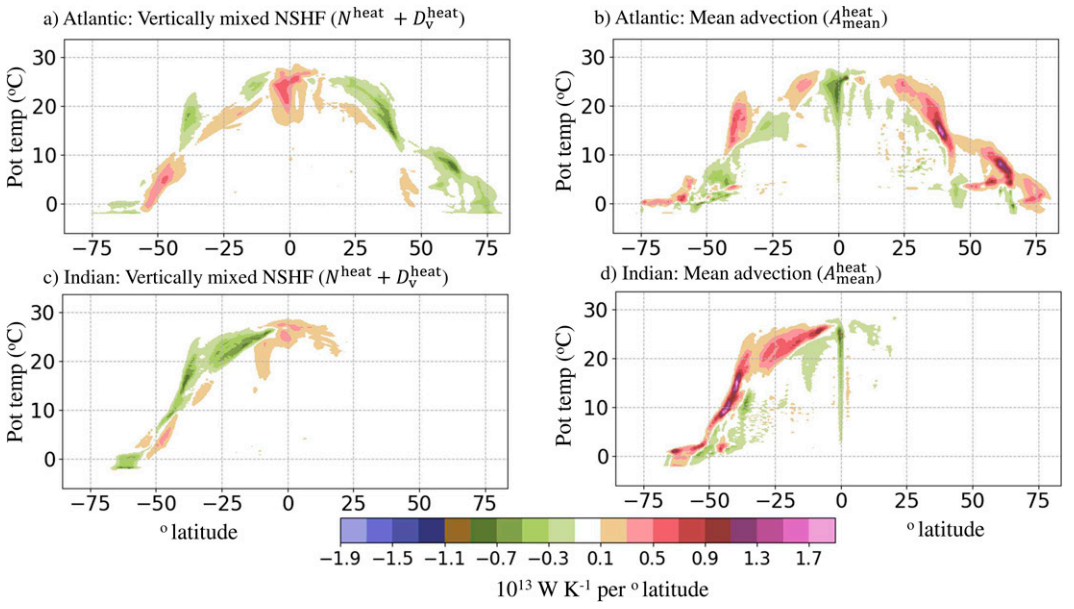

FIG. 9. Mean net heat flux terms from the LL control integration over 2000–09.

The corresponding pattern is much less marked in $N^{salt} + D_v^{salt}$ and is not discernible in A_{mean}^{salt}.

In potential density space, (ϕ, ρ), the isopycnal diffusion term D_{iso}^{dens} is small (it is not exactly zero for several reasons). So $N^{dens} + D_v^{dens}$ and A_{full}^{dens} are very strongly anticorrelated, and $N^{dens} + D_v^{dens}$ and $A_{full}^{dens} - A_{rect}^{dens}$ are more strongly anticorrelated than they are for θ. Figure 12 presents the patterns of $N^{dens} + D_v^{dens}$ and $A_{full}^{dens} - A_{rect}^{dens}$ in the Pacific and Atlantic Oceans for the LL integrations. Potential density varies much more slowly with θ in cold water than warm water so the arms of the horseshoe shape in the upper panels of Figs. 8 and 9 are compressed in Fig. 12 as well as inverted (because density decreases as temperature increases). As anticipated, in both basins the patterns in $N^{dens} + D_v^{dens}$ are well anticorrelated with those of $A_{full}^{dens} - A_{rect}^{dens}$.

Figures 13a and 13b provide a convenient summary of the pattern correlation coefficients in $(\phi$, class) space calculated using (11) between $N + D_v$ and A_{mean} for each of the three classes and three main basins in the LL and MM integrations; for salinity and density A_{mean} is calculated from $A_{full} - A_{rect}$

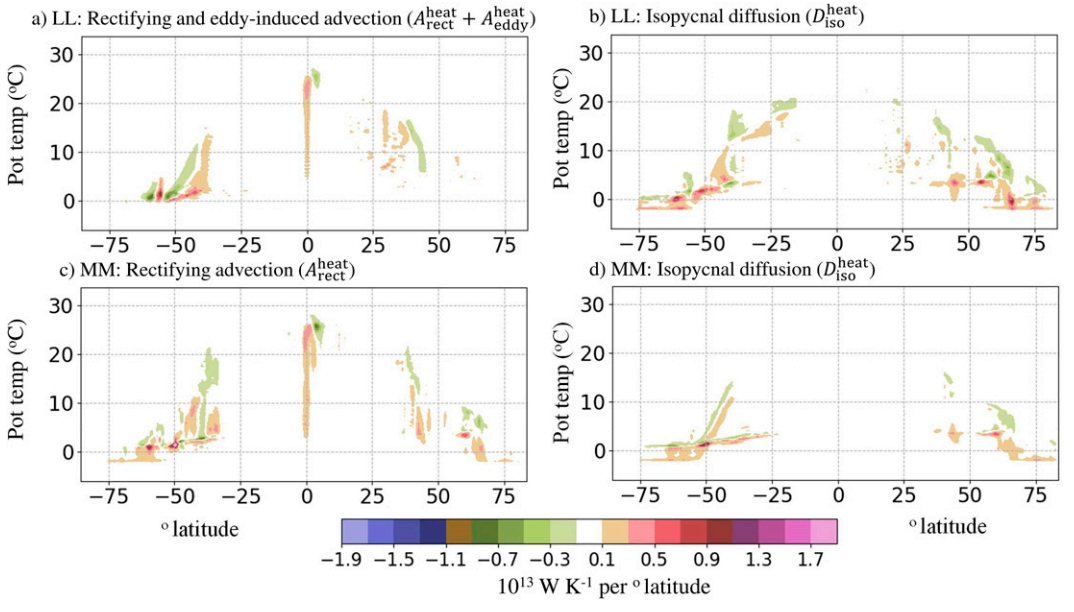

FIG. 10. Mean net heat flux terms for the Atlantic Ocean from the LL and MM control integrations over 2000–09.

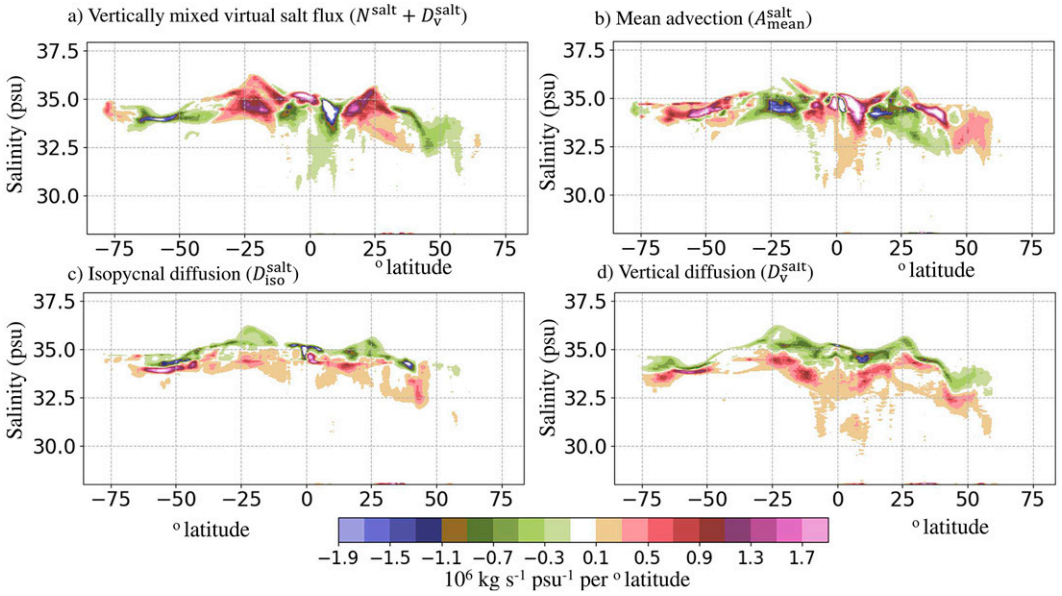

FIG. 11. Mean net salt flux divergence terms for the Pacific from the LL control integration over 2000–09 as a function of latitude and salinity.

while for heat it is calculated from $A_{full} - A_{rect} - A_{eddy}$. The magnitude of the correlations is clearly largest for ρ (>0.85), smallest for S (between 0.6 and 0.7) and between 0.75 and 0.85 for θ. It varies somewhat depending on the ocean basin and the model resolution. Comparison of Figs. 13c and 13a shows that the magnitude of the correlation between $N + D_v$ and A_{full} is slightly greater than that between $N + D_v$ and A_{mean} for S and θ and considerably greater for ρ. Comparison of Figs. 13d and 13a shows that the magnitudes of the correlations between $N^{heat} + D_v^{heat}$ and A_{mean}^{heat} are somewhat increased when the region considered is restricted to that within 45° of the equator.

d. How much spurious mixing is produced by advection?

In a Boussinesq rigid-lid model (e.g., Gordon et al. 2000; Gregory 2000) the integral $I_A(\tau_0)$ of the divergence of the advective flux of any tracer τ over a volume $\mathcal{V}_0$ where $\tau(x, y, z) > \tau_0$, that is bounded by the part of the air–sea interface where $\tau > \tau_0$, land boundaries and the isopleth $\tau = \tau_0$, should be zero. This result is derived in two steps. First, a rigid-lid model

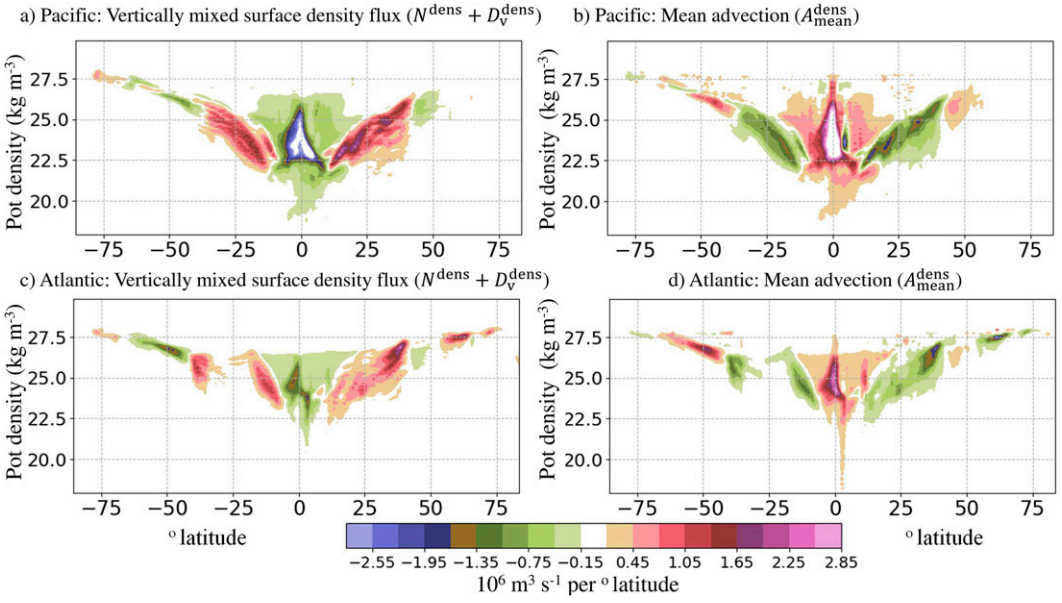

FIG. 12. Mean net potential density flux divergence terms from the LL control integration over 2000–09 as a function of latitude and potential density.

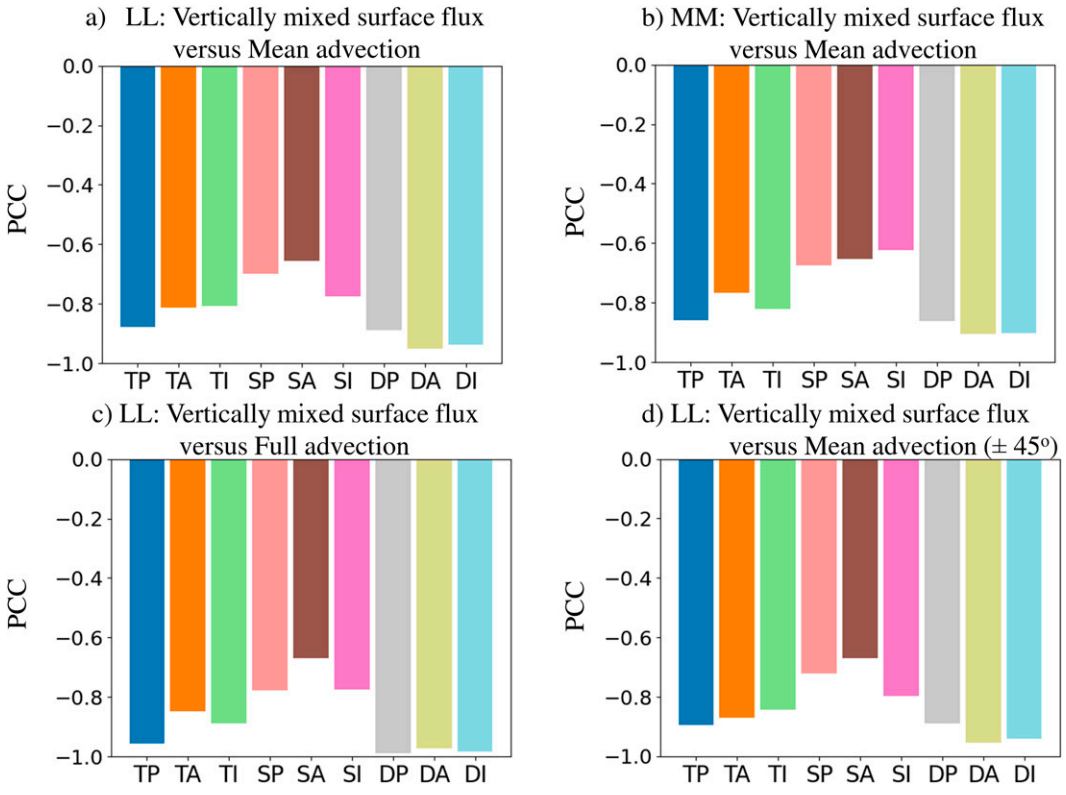

FIG. 13. The pattern correlation coefficients (PCC) in (latitude, class) space calculated using (11) for the terms $N + D_v$ and A_{mean} for (a) the LL and (b) the MM integrations. Pattern correlations as in (a), but for (c) the terms $N + D_v$ and A_{full} and (d) restricting the latitudes to within 45° of the equator. The first letter, T, S, or D, on the abscissa indicates the class: potential temperature, salinity, or density, respectively. The second letter, P, A, or I, indicates the Pacific, Atlantic, or Indian Ocean basins, respectively.

requires there to be no flow across the air–sea interface, so I_A depends only on the flux across the isopleth:

$$I_A(\tau_0) \equiv -\int_{\mathcal{V}_0} \nabla\cdot(\tau\mathbf{u})d\mathcal{V} = -\tau_0\int_{\partial\mathcal{V}_0^{\tau_0}} \mathbf{u}\cdot\hat{\mathbf{n}}d\mathcal{S}, \tag{13}$$

with $\partial\mathcal{V}_0^{\tau_0}$ denoting the part of the boundary where $\tau = \tau_0$. Second, by the Boussinesq assumption the flow is incompressible within $\mathcal{V}_0$, and since there is no volume flow across the air–sea interface or land boundaries there can be none across the isopleth $\partial\mathcal{V}_{0\tau_0}$. So the final term on the rhs of (13) is zero, and $I_A(\tau_0) = 0$.

In such a model, any deviations of $I_A(\tau_0)$ from zero can be ascribed to numerical mixing: i.e., different choices of τ in calculating the model advective flux at different cell faces making up the discrete representation of $\partial\mathcal{V}_{0\tau_0}$.

However, modern ocean models such as the NEMO v3.6 configuration diagnosed here allow a fully nonlinear free surface in which mass flux is permitted across the air–sea interface [see (5)], and the cell thicknesses vary as the free surface height changes. In such models $I_A(\tau_0) \neq 0$, even without numerical mixing. We show in the appendix that for our model

$$I_A(\theta_0) = \theta_0\left[\int_{\partial\mathcal{V}_0^{\text{asi}}} e_V d\mathcal{S} + \int_{\mathcal{V}_0}\frac{1}{e_3}\frac{\partial e_3}{\partial t}d\mathcal{V}\right], \tag{14}$$

$$I_A(S_0) = S_0\left[\int_{\partial\mathcal{V}_0^{\text{asi}}} e_V d\mathcal{S} + \int_{\mathcal{V}_0}\frac{1}{e_3}\frac{\partial e_3}{\partial t}d\mathcal{V}\right] - \int_{\partial\mathcal{V}_0^{\text{asi}}} e_V S d\mathcal{S}. \tag{15}$$

Here $\partial\mathcal{V}_0^{\text{asi}}$ denotes the boundary of $\mathcal{V}_0$ at the air–sea interface. The expected value of A_{full} for the heat budget is $c_p\rho_0 I_A(\theta_0)$ while that for the salt budget is $0.001\rho_0 I_A(S_0)$. The extra term on the rhs of (15) arises from the fact that the heat content of the water passing through the air–sea interface is considered as part of the NSHF term, but the salt flux Se_V passing through it associated with the volume flux e_V in (5) is assigned to the advection term (A^{salt}) when the virtual salt flux N^{salt} is subtracted from the original advection term.

Our discussion follows Holmes et al. (2019a) and Holmes et al. (2021), who use similar integrals to provide insights into the potential weaknesses of their model configurations, but is limited by the fact that we have only been able to assign accumulated terms from the tracer equations to tracer classes using monthly mean tracer values. The integrals for the total advection term will contain errors because of this, but the

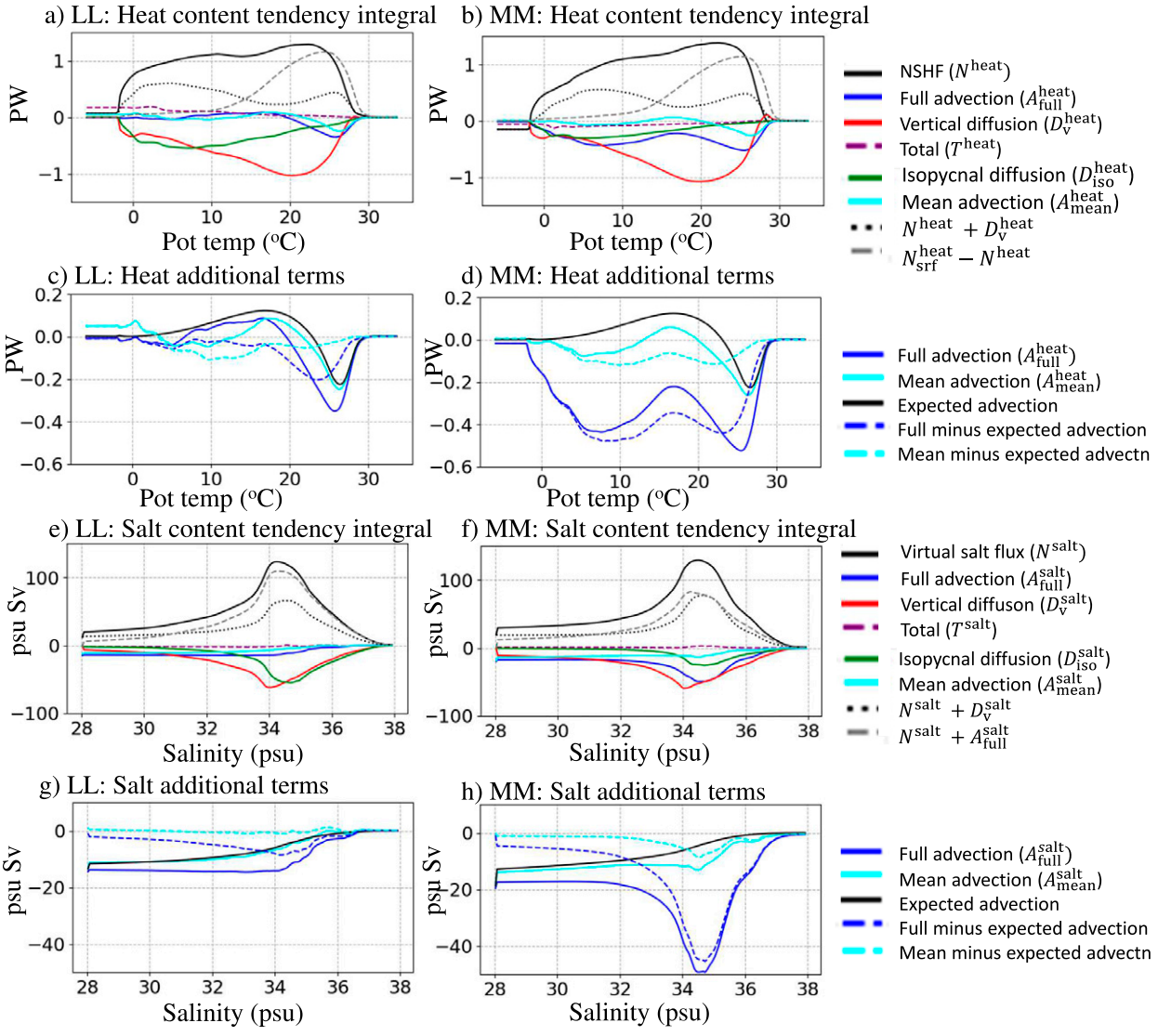

FIG. 14. (a)–(d) Integrals of heat content tendency terms over all points in the global domain where $\theta > \theta_0$; θ_0 is the abscissa. (e)–(h) Integrals of salt content tendency terms over all points in the global domain where $S > S_0$; S_0 is the abscissa. Results shown for the (left) LL and (right) MM control integrations. The expected values are calculated using (14) and (15).

advection by the monthly mean flow of the monthly mean tracer field should satisfy (14) or (15).

Figures 14a–d present the integrals, over all the points in the global domain where $\theta > \theta_0$, of a number of heat content tendency terms from the LL (left) and MM (right) integrations. Figure 14a shows that in the LL integration there is a global NSHF N^{heat} of about 1.3 PW (full black line) for $\theta_0 > 23$°C and that about two-thirds of this heat is lost in waters with $\theta_0 < 0$°C. Vertical diffusion D^{heat}_{v} (red line) redistributes this heat, offsetting the input by N^{heat}, so that their sum, $N^{heat} + D^{heat}_{v}$ (dotted black line), is relatively modest, compared to N^{heat}, for $\theta_0 > 15$°C. The difference in heat input due to the penetration of solar radiation, $N^{heat}_{srf} - N^{heat}$ (gray dashed line) is substantial for $\theta_0 > 15$°C. Were all solar radiation absorbed at the surface, the net heat input would be the sum of N^{heat} and $N^{heat}_{srf} - N^{heat}$ and exceed 2.2 PW for $\theta_0 > 25$°C. Isopycnal diffusion D^{heat}_{iso} (green line) and full advection A^{heat}_{full} (blue line) together oppose $N^{heat} + D^{heat}_{v}$. The total tendency T^{heat} (purple dashed line) is fairly close to zero but has a noticeable input of heat at around $\theta_0 = 4$°C and a global net imbalance of about 0.15 PW.

The full advection and the mean advection A^{heat}_{mean} (full cyan line) are nonzero, with the peak discrepancy occurring just above 25°C. The black line in Fig. 14c is the expected value for the advection term $c_p \rho_0 I_A(\theta_0)$ calculated using (14). The dashed lines in Fig. 14c are the integrals of A^{heat}_{full} (blue) and A^{heat}_{mean} (cyan) with this expected value subtracted. One sees that the error in A^{heat}_{mean} is quite small and that the error in A^{heat}_{full} is smaller than one would infer if (14) were not taken into account. Figures 14b and 14d show the corresponding

results for the MM integration. One sees that the D^{heat}_{iso} term is reduced by about a half (its coefficients have been reduced by a factor of 6) and A^{heat}_{full} is significantly larger than in the LL integration, though as mentioned earlier our calculation does not allow us to firmly conclude that this is due to spurious advection. Figure 14d also shows that the error in A^{heat}_{mean} (dashed cyan) is still small.

Figures 14e–h present the corresponding results to Figs. 14a–d for contributions to the rate of change of salt content by salinity class. The line colors and styles in Figs. 14e and 14f match those in Figs. 14a and 14b except that the gray dashed lines in Figs. 14e and 14f are the sum of the advection and net surface flux terms, $A^{salt}_{full} + N^{salt}$. Noting that T^{salt} (purple dashed line) is small, (3) implies that $A^{salt}_{full} + N^{salt}$ must be almost equal and opposite to $D^{salt}_{iso} + D^{salt}_{v}$. Diffusion terms are expected to flux salt from smaller and larger values toward intermediate values. So their integrals in Fig. 14 are expected to have negative values consistent with both the D^{salt}_{iso} (green) and D^{salt}_{v} (red) lines. In both Figs. 14g and 14h, the expected value for the integral of A^{salt}_{full} (black line) agrees well with the integral of A^{salt}_{mean} (solid cyan). Its agreement with the integral of the full advection term (A^{salt}_{full}, solid blue) is good in the LL integration and significantly less good in the MM integration, leaving an appreciable difference between them (blue dashed line).

e. *What are the main sources of the heat lost in the North Atlantic?*

Figure 3 presents the sums over all classes of the net heat and salinity flux divergences by full advection (A_{full}) and surface fluxes (N_{srf}) for a number of latitude bands in each ocean basin. To within machine precision, D_v and $N - N_{srf}$ are zero for these quantities, so the values for N_{srf} are the same as those for N and $N + D_v$. Comparison of Figs. 3b and 3e and of Figs. 3c and 3f shows that these sums of N^{heat} and A^{heat}_{full} are almost equal and opposite in the LL and MM integrations, respectively. Figures 3e and 3f show that the latitude band sums of A^{heat}_{full} are also rather similar in the LL and MM integrations, the most notable differences being in the Indian Ocean. In the Indian Ocean, it is clear that in the LL integration more heat is lost to the atmosphere (between 45° and 15°S) than is gained (between 15°S and 15°N). This is much less pronounced in the MM integration. The dominance of the equatorial Pacific regions in the 2.3 PW of annual mean ocean heat uptake (Forget and Ferreira 2019) is particularly marked in the LL integration (Fig. 3b). The latitude band sums of A^{heat}_{mean} (not shown) and A^{heat}_{full} are rather similar. Figure 3g (whose ordinate has been rescaled) shows that $A^{heat}_{rect} + A^{heat}_{eddy}$ cools the equatorial belt and that its latitude band sums, like those of D^{heat}_{iso} (not shown), are about a factor of 10 smaller than those of A^{heat}_{full} and N^{heat}. These sums of D^{heat}_{iso} and $A^{heat}_{rect} + A^{heat}_{eddy}$ have a tendency to cancel each other, particularly south of 30°S.

Figures 3h and 3i show corresponding results to Figs. 3e and 3b for the A^{salt}_{full} and N^{salt} saline flux divergences. Precipitation, evaporation, and river inflow make the subtropical gyres (between 15° and 30° in both the Southern and Northern Hemispheres) more salty and the equatorial and high latitudes less salty. The terms A^{salt}_{full} and $-N^{salt}$ are again very similar, the largest differences being in the 60°–45°S band. The term A^{salt}_{full} in the MM integration (not shown) is also similar to the LL integration, the largest differences being in the Atlantic in the equatorial and 60°–45°S bands.

Returning to Fig. 3c, one sees that the heat lost in the Atlantic north of 60°N is much greater than the heat input into the Atlantic and Indian Oceans between 60° and 45°S. This is contrary to what the schematic presented in Fig. 4 suggests but potentially consistent with the analysis of Talley (2013), Forget and Ferreira (2019), and Holmes et al. (2019b). Figure 15 allows this issue to be investigated in some detail. It shows the heat input by $N^{heat} + D^{heat}_{v}$ (red solid), A^{heat}_{full} (green solid), and A^{heat}_{mean} (blue dashed) for each basin and selected latitude bands. We have seen (Fig. 14c) that the global error in A^{heat}_{mean} is relatively small, and one can see from Fig. 15c that except for water colder than about 2°C, the global values of $N^{heat} + D^{heat}_{v}$ and A^{heat}_{mean} as a function of θ are approximately equal and opposite. One can consider for a given θ which regions take up the heat lost in other regions. None of the regions has a net loss of heat ($N^{heat} + D^{heat}_{v}$) with $\theta > 26$°C, and there is a global net heat input for $\theta > 26$°C clearly apparent in Fig. 15c. The heat lost between 20° and 25°C in the North Atlantic and the southern and equatorial Indian Ocean is mainly compensated by heat taken up in the equatorial Pacific and equatorial Atlantic but there is a small heat loss globally at these potential temperatures. Figure 15b shows that the North Atlantic loses about 0.03 PW K^{-1} of heat fairly uniformly for θ between 0° and 20°C. Figures 15j–l show that the Pacific is the only ocean that has a net uptake of heat for θ between 8° and 20°C. Figure 15c shows that this uptake of heat in the Pacific exceeds the heat loss in the Atlantic and Indian Oceans. Figures 15d and 15e respectively show that the range of θ warmed in the equatorial Pacific extends down as far as 5°C, and that it only extends down to about 13°C in the equatorial Atlantic. The southern Pacific, Atlantic, and Indian Oceans take up heat for θ between 8° and 13°C, between 0° and 10°C, and between 2° and 8°C, respectively. This uptake of heat must be obscured in Fig. 3c by heat loss in other θ ranges.

In conclusion, the differences between the heat uptake in the equatorial Pacific, Atlantic, and Indian Oceans, evident in Figs. 15d–f, are as large as the more well-known differences between the heat lost in the North Atlantic and Pacific Oceans (Figs. 15a,b). The net heat uptake by the Pacific (Fig. 15j) plays a major role in feeding the heat lost over a wide range of potential temperatures in the Indian and Atlantic Oceans (Figs. 15k,l), and the heat uptake in the equatorial Pacific (Fig. 15c) makes a significant contribution to the heat lost in the North Atlantic (Fig. 15b).

4. Concluding summary and discussion

The decadal mean NSHF for 2000–09 from the low-resolution HadGEM3-GC3.1 hist-1950 integration has been shown (Fig. 1) to agree well with the DEEP-C reanalysis products for the same period. The NSHFs for this coupled climate model are also relatively insensitive to resolution (see Fig. 2), the main differences being in the North Atlantic and Agulhas Retroflection regions where the NSHFs from the higher-resolution simulations agree better with the DEEP-C reanalyses. We have taken this

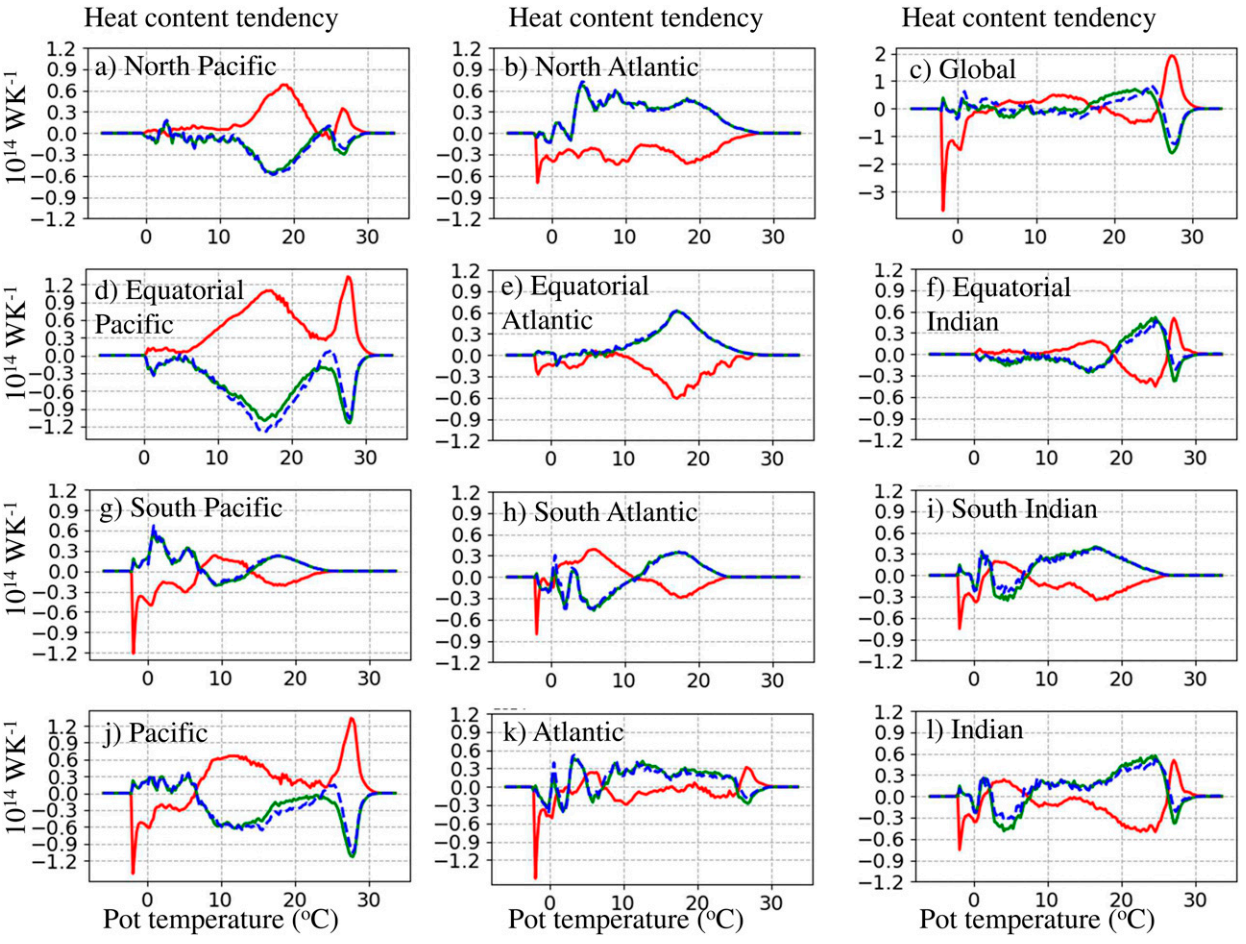

FIG. 15. Net heat input as a function of potential temperature by $N^{\text{heat}} + D_v^{\text{heat}}$ (red solid), $A_{\text{full}}^{\text{heat}}$ (green solid), and $A_{\text{mean}}^{\text{heat}}$ (blue dashed) for selected basins and latitude bands. The equatorial regions extend from 30°S to 30°N.

opportunity to outline a relatively simple dynamical interpretation of the geographical patterns of the NSHFs visible in Fig. 1 in which cooling of the near-surface by wind-driven Ekman upwelling, the influence of boundary waves in reducing along-boundary density gradients, and heat input to higher latitudes from poleward advection by the time-mean flow all play prominent roles. Our interpretation suggests that Ekman upwelling is a key element in regions of net surface heat input to the ocean and that advection by the time-mean flow is a key element in regions of heat loss to the atmosphere.

As a step in the investigation of the validity and limitations of this interpretation, we have examined the main terms (see Table 2) in the time-mean tracer budgets in this climate model for potential temperature, salinity, and potential density in the main ocean basins. We have shown in section 3b that nearly all the contributions from vertical mixing occur in a near-surface layer that is either within 100 m of the surface or within 1.2 times the monthly maximum mixed layer depth (Fig. 6). Plotting the heat budget terms as a function of latitude and potential temperature, we have shown in section 3c that the sum of the net surface heat flux and vertical mixing terms (N^{heat} and D_v^{heat}, respectively) is closely balanced by the full advection ($A_{\text{full}}^{\text{heat}}$) and mainly balanced by the time-mean advection ($A_{\text{mean}}^{\text{heat}}$) in each of the basins. This supports the two assumptions made by ventilated thermocline theory: that water mass transformations occur "near (the) surface" and that following the time-mean motion, tracers are mainly changed by these near-surface transformations. Our interpretation of the surface fluxes follows the spirit of the surface stream-function concept (Marsh 2000) while recognizing that the modification of the surface heat fluxes by the penetration of solar radiation and near-surface vertical mixing is very significant. The balance between $N + D_v$ and A_{mean} holds more closely for potential density and less closely for salinity than it does for potential temperature (see Fig. 13) suggesting that a similar interpretation of the surface fluxes applies well for potential density and is much less satisfactory for salinity.

We have also shown that the simple schematic of Fig. 4 does not capture the main terms in the heat budget in some geographical regions. At high latitudes in the Southern Ocean and the North Atlantic, isopycnal diffusion and/or transports by the time-varying flow are significant. These limitations are consistent with expectations based on Gregory (2000) and

Gent (2016). Very close to the equator, transports by the time-varying flow $A_{\text{rect}}^{\text{heat}}$, (e.g., by tropical instability waves) significantly reduce the cooling by the time-mean advection.

It is well known that the net heat input by advection to any potential temperature class summed over all latitudes should be close to zero (Walin 1982). We have calculated a residual value (14) that arises from fluxes of freshwater across the air–sea interface and shown that this correction should not be neglected (Fig. 14). We have also presented results on the net heat inputs by latitude bands summed over all potential temperature classes. These inputs are identically zero for vertical diffusion. We have shown that they are dominated by a balance between the NSHF and the advection (see Fig. 3). We have also argued that the heat taken up in the equatorial Pacific makes a significant contribution to the heat lost in the North Atlantic (Fig. 15) supporting the analysis of Talley (2013), Forget and Ferreira (2019), and Holmes et al. (2019b).

We have argued that tracer advection is very important in the heat budget and MOCs, despite the restrictions on it imposed by the mathematical fact that, in a seasonally varying equilibrium, it must be very close to zero in global integrals over tracer classes. McWilliams et al. (1996) examined the conundrum that arises if one supposes that the diapycnal mixing across a low-latitude "warm water" volume bounded by an isotherm, such as the 20°C isotherm, could not be strong enough to balance the NSHF input. They found that the diapycnal mixing in their (coarse resolution) model did balance the NSHF. It may be helpful to consider this issue from the perspective in which it is assumed that surface fluxes, near-surface vertical mixing and advection are the only processes involved in the heat budget. Cold water driven toward the surface near the equator by the winds is only warmed when it reaches the region where there is surface heat input or vertical mixing of that heat input. In the absence of the NSHF, the water advected away to other latitudes would have the same temperature as it did when it was advected into the region, and there would be no net advective heat input. Similarly, as the water near the surface is advected to higher latitudes, it will only change its temperature when it is cooled by the NSHF (or water from below is mixed vertically into it). In this sense the advective term in the heat budget is totally dependent on the NSHF (and mixing processes). If one considers only the heat budget, its terms appear to have a curiously elusive, "chicken and egg" nature. This argument is also relevant to the assessment of the importance of the impact of ocean biology on the parameterization of the solar penetration (Murtugudde et al. 2002). Changes to the penetration of solar radiation can give large local changes in the differences between the model and observations but their impacts on the heat budget in potential temperature space would be more subtle.

One of the limitations of our study is that we have not accumulated terms by tracer class on the fly at every time step. That would enable better calculation of global budgets by tracer class. We believe that it would be possible to implement this in a modular and sustainable manner. The accumulation of these diagnostics would require the relevant decades of the model integration to be repeated and would increase the size of the diagnostic outputs as the data would be saved as 3D fields. On-the-fly accumulation of vertical mixing contributions within and just outside the surface mixed layer would also need to be carefully considered.

This paper has only touched on one aspect of the interpretation of coupled model simulations in the light of conceptual models of MOCs. Other investigations that would complement this study include ones on variations in the depths of isopycnals along the eastern (and western) boundaries of the major ocean basins, relationships between zonal-mean wind stresses and NSHFs in the equatorial regions, and relationships between isothermal and isopycnal depths on eastern boundaries and heat fluxes into northern basins. Whether the diagnostics presented in this paper are more relevant to the upper ocean on time scales shorter than a century and less relevant to the deep ocean on much longer time scales may also deserve further investigation. Although the relationships between net surface fluxes and MOCs in coupled "control" integrations are of interest in their own right, the primary aim of our studies is to develop diagnostics that provide useful insights into simulations of climate change.

Acknowledgments. Bell and Storkey were supported by the Met Office Hadley Centre Climate Programme funded by BEIS. Nurser acknowledges support from the NERC project CLASS (NE/R015953/1). The authors gratefully acknowledge contributions from Pat Hyder, suggestions from David Marshall, and advice from Chunlei Lui and Richard Allan.

Data availability statement. The code and input data used to generate the figures are available from Bell et al. (2023).

APPENDIX

Calculation of the Integral of the Advection Term over a Domain Bounded by a Tracer Isopleth

We start our derivations of (14) and (15) from the tracer advection equation obtained from (1) and (2) by setting $(D_v)_{ijk} = (D_{\text{iso}})_{ijk} = N_{ijk} = 0$, dividing by $e_1e_2e_3$ and recognizing that e_1 and e_2 are independent of k and t:

$$\frac{1}{e_1e_2e_3}\left[\frac{\partial(e_2e_3u\tau)}{\partial i}+\frac{\partial(e_1e_3v\tau)}{\partial j}+\frac{\partial(e_1e_2\omega\tau)}{\partial k}\right] = -\frac{1}{e_1e_2e_3}\frac{\partial(e_1e_2e_3\tau)}{\partial t} = -\frac{1}{e_3}\frac{\partial(e_3\tau)}{\partial t}. \tag{A1}$$

We note for use below that the model's continuity equation can be obtained by setting $\tau = 1$ in (A1), that the volume of a gridcell element $d\mathcal{V}$ is indeed given by $d\mathcal{V} = e_1e_2e_3\,di\,dj\,dk$, and that the upward vertical velocity across the s-coordinate at the free surface, ω_s, is given by

$$\omega_s = e_V, \tag{A2}$$

where e_V is defined in (5).

Integrating (A1) over the volume $\mathcal{V}_0$ used to define $I_A(\tau_0)$ in (13), using the divergence theorem and (A2) we obtain

$$I_A(\tau_0) = -\tau_0 \int_{\partial\mathcal{V}_0^{\tau_0}} \mathbf{u}\cdot\hat{\mathbf{n}}\, d\mathcal{S} - \int_{\partial\mathcal{V}_0^{\text{asi}}} \tau_{\text{asi}} e_V\, d\mathcal{S}. \tag{A3}$$

In our model the rate of change of heat content of the ocean associated with the water crossing the interface is treated as a surface flux. So $\tau_{\text{asi}} = 0$ in the calculation of the tracer advection for both potential temperature and salinity, and the second of the two terms on the rhs of (A3) is zero. Using the continuity equation [i.e., (A1) with $\tau = 1$], integrating over the volume $\mathcal{V}_0$, one can show that

$$-\int_{\partial\mathcal{V}_0^{\tau_0}} \mathbf{u}\cdot\hat{\mathbf{n}}\, d\mathcal{S} = \int_{\mathcal{V}_0} \frac{1}{e_3}\frac{\partial e_3}{\partial t}\, d\mathcal{V} + \int_{\partial\mathcal{V}_0^{\text{asi}}} e_V\, d\mathcal{S}. \tag{A4}$$

Substituting (A4) in (A3) and setting $\tau = \theta$ one obtains (14). Subtracting the surface virtual salt flux, $1000N^{\text{salt}}/\rho_0$, from (A3), setting $\tau = S$ and using (5)–(7) one obtains (15).

REFERENCES

Abernathey, R., J. Marshall, and D. Ferreira, 2011: The dependence of Southern Ocean meridional overturning on wind stress. *J. Phys. Oceanogr.*, **41**, 2261–2278, https://doi.org/10.1175/JPO-D-11-023.1.

Adcroft, A., and J.-M. Campin, 2004: Rescaled height coordinates for accurate representation of free surface flows in ocean circulation models. *Ocean Modell.*, **7**, 269–284, https://doi.org/10.1016/j.ocemod.2003.09.003.

Bell, M. J., 2015a: Meridional overturning circulations driven by surface wind and buoyancy forcing. *J. Phys. Oceanogr.*, **45**, 2701–2714, https://doi.org/10.1175/JPO-D-14-0255.1.

——, 2015b: Water mass transformations driven by Ekman upwelling and surface warming in sub-polar gyres. *J. Phys. Oceanogr.*, **45**, 2356–2380, https://doi.org/10.1175/JPO-D-14-0251.1.

——, A. J. G. Nurser, and D. Storkey, 2023: Interpretation of net surface heat fluxes and meridional overturning circulations in global coupled UK-HadGEM3 climate simulations (1.0). Zenodo, https://doi.org/10.5281/zenodo.7766255.

Broecker, W. S., 1991: The Great Ocean Conveyor. *Oceanography*, **4**, 79–89, https://doi.org/10.5670/oceanog.1991.07.

Bryden, H. L., and E. C. Brady, 1989: Eddy momentum and heat fluxes and their effects on the circulation of the equatorial Pacific Ocean. *J. Mar. Res.*, **47**, 55–79.

Dias, F. B., C. M. Domingues, S. J. Marsland, S. M. Griffies, S. R. Rintoul, R. Matear, and R. Fiedler, 2020: On the superposition of mean advective and eddy-induced transports in global ocean heat and salt budgets. *J. Climate*, **33**, 1121–1140, https://doi.org/10.1175/JCLI-D-19-0418.1.

Exarchou, E., T. Kuhlbrodt, J. M. Gregory, and R. S. Smith, 2015: Ocean heat uptake processes: A model intercomparison. *J. Climate*, **28**, 887–908, https://doi.org/10.1175/JCLI-D-14-00235.1.

Ferreira, D., and Coauthors, 2018: Atlantic-Pacific asymmetry in deep water formation. *Annu. Rev. Earth Planet. Sci.*, **46**, 327–352, https://doi.org/10.1146/annurev-earth-082517-010045.

Forget, G., and D. Ferreira, 2019: Global ocean heat transport dominated by heat export from the tropical Pacific. *Nat. Geosci.*, **12**, 351–354, https://doi.org/10.1038/s41561-019-0333-7.

Fox-Kemper, B., and Coauthors, 2021: Ocean, cryosphere and sea level change. *Climate Change 2021: The Physical Science Basis*, V. Masson-Delmotte et al., Eds., Cambridge University Press, 1211–1362, https://doi.org/10.1017/9781009157896.011.

Gaspar, P., Y. Grégoris, and J.-M. Lefevre, 1990: A simple eddy kinetic energy model for simulations of the oceanic vertical mixing: Tests at station papa and long-term upper Ocean study site. *J. Geophys. Res.*, **95**, 16 179–16 193, https://doi.org/10.1029/JC095iC09p16179.

Gent, P. R., 2016: Effects of southern hemisphere wind changes on the meridional overturning circulation in ocean models. *Annu. Rev. Mar. Sci.*, **8**, 79–94, https://doi.org/10.1146/annurev-marine-122414-033929.

——, and J. C. McWilliams, 1990: Isopycnal mixing in ocean circulation models. *J. Phys. Oceanogr.*, **20**, 150–155, https://doi.org/10.1175/1520-0485(1990)020<0150:IMIOCM>2.0.CO;2.

Gnanadesikan, A., 1999: A simple predictive model of the structure of the oceanic pycnocline. *Science*, **283**, 2077–2079, https://doi.org/10.1126/science.283.5410.2077.

——, R. D. Slater, P. S. Swathi, and G. K. Vallis, 2005: The energetics of ocean heat transport. *J. Climate*, **18**, 2604–2616, https://doi.org/10.1175/JCLI3436.1.

Good, S. A., M. J. Martin, and N. A. Rayner, 2013: EN4: Quality controlled ocean temperature and salinity profiles and monthly objective analyses with uncertainty estimates. *J. Geophys. Res. Oceans*, **118**, 6704–6716, https://doi.org/10.1002/2013JC009067.

Gordon, A. L., 1986: Interocean exchange of thermocline water. *J. Geophys. Res.*, **91**, 5037–5046, https://doi.org/10.1029/JC091iC04p05037.

Gordon, C., C. Cooper, C. A. Senior, H. Banks, J. M. Gregory, T. C. Johns, J. F. B. Mitchell, and R. A. Wood, 2000: The simulation of SST, sea ice extents and ocean heat transports in a version of the Hadley Centre coupled model without flux adjustments. *Climate Dyn.*, **16**, 147–168, https://doi.org/10.1007/s003820050010.

Graham, T., 2014: The importance of eddy permitting model resolution for simulation of the heat budget of tropical instability waves. *Ocean Modell.*, **79**, 21–32, https://doi.org/10.1016/j.ocemod.2014.04.005.

Gregory, J. M., 2000: Vertical heat transports in the ocean and their effect on time-dependent climate change. *Climate Dyn.*, **16**, 501–515, https://doi.org/10.1007/s003820000059.

——, and Coauthors, 2016: The Flux-Anomaly-Forced Model Intercomparison Project (FAFMIP) contribution to CMIP6: Investigation of sea-level and ocean climate change in response to CO_2 forcing. *Geosci. Model Dev.*, **9**, 3993–4017, https://doi.org/10.5194/gmd-9-3993-2016.

Griffies, S. M., and Coauthors, 2015: Impacts on ocean heat from transient mesoscale eddies in a hierarchy of climate models. *J. Climate*, **28**, 952–977, https://doi.org/10.1175/JCLI-D-14-00353.1.

Grist, J. P., S. A. Josey, R. Marsh, Y.-O. Kwon, R. J. Bingham, and A. T. Blaker, 2014: The surface-forced overturning of the North Atlantic: Estimates from modern era atmospheric reanalysis datasets. *J. Climate*, **27**, 3596–3618, https://doi.org/10.1175/JCLI-D-13-00070.1.

Groeskamp, S., and D. Iudicone, 2018: The effect of air-sea flux products, shortwave radiation, depth penetration, and albedo on the upper ocean overturning circulation. *Geophys. Res. Lett.*, **45**, 9087–9097, https://doi.org/10.1029/2018GL078442.

——, S. M. Griffies, D. Iudicone, R. Marsh, A. J. G. Nurser, and J. D. Zika, 2019: The water mass transformation framework for ocean physics and biogeochemistry. *Annu. Rev. Mar. Sci.*,

11, 271–305, https://doi.org/10.1146/annurev-marine-010318-095421.

Held, I. M., and V. D. Larichev, 1996: A scaling theory for horizontally homogeneous, baroclinically unstable flow on a beta plane. *J. Atmos. Sci.*, **53**, 946–952, https://doi.org/10.1175/1520-0469(1996)053<0946:ASTFHH>2.0.CO;2.

Hewitt, H. T., and Coauthors, 2017: Will high-resolution global ocean models benefit coupled predictions on short-range to climate timescales? *Ocean Modell.*, **120**, 120–136, https://doi.org/10.1016/j.ocemod.2017.11.002.

Hieronymus, M., and J. Nycander, 2013: The budgets of heat and salinity in NEMO. *Ocean Modell.*, **67**, 28–38, https://doi.org/10.1016/j.ocemod.2013.03.006.

Holmes, R. M., J. D. Zika, and M. H. England, 2019a: Diathermal heat transport in a global ocean model. *J. Phys. Oceanogr.*, **49**, 141–161, https://doi.org/10.1175/JPO-D-18-0098.1.

——, ——, R. Ferrari, A. F. Thompson, E. R. Newsom, and M. H. England, 2019b: Atlantic Ocean heat transport enabled by Indo-Pacific heat uptake and mixing. *Geophys. Res. Lett.*, **46**, 13 939–13 949, https://doi.org/10.1029/2019GL085160.

——, ——, S. M. Griffies, A. M. Hogg, A. E. Kiss, and M. H. England, 2021: The geography of numerical mixing in a suite of global ocean models. *J. Adv. Model. Earth Syst.*, **13**, e2020MS002333, https://doi.org/10.1029/2020MS002333.

Huang, R. X., 2010: *Ocean Circulation: Wind-Driven and Thermohaline Processes*. Cambridge University Press, 791 pp.

Hughes, C. W., J. Williams, A. Blaker, A. Coward, and V. Stepanov, 2018: A window on the deep ocean: The special value of ocean bottom pressure for monitoring the large-scale, deep-ocean circulation. *Prog. Oceanogr.*, **161**, 19–46, https://doi.org/10.1016/j.pocean.2018.01.011.

Hyder, P., and Coauthors, 2018: Critical Southern Ocean climate model biases traced to atmospheric model cloud errors. *Nat. Commun.*, **9**, 3625, https://doi.org/10.1038/s41467-018-05634-2.

Iudicone, D., G. Madec, and T. J. MacDougall, 2008a: Water-mass transformations in a neutral density framework and the key role of light penetration. *J. Phys. Oceanogr.*, **38**, 1357–1376, https://doi.org/10.1175/2007JPO3464.1.

——, S. Speich, G. Madec, and B. Blanke, 2008b: The global conveyor belt from a Southern Ocean perspective. *J. Phys. Oceanogr.*, **38**, 1401–1425, https://doi.org/10.1175/2007JPO3525.1.

Jackson, L. C., and Coauthors, 2020: Impact of ocean resolution and mean state on the rate of AMOC weakening. *Climate Dyn.*, **55**, 1711–1732, https://doi.org/10.1007/s00382-020-05345-9.

Johnson, H. L., P. Cessi, D. P. Marshall, F. Schloesser, and M. A. Spall, 2019: Recent contributions of theory to our understanding of the Atlantic meridional overturning circulation. *J. Geophys. Res. Oceans*, **124**, 5376–5399, https://doi.org/10.1029/2019JC015330.

Kara, A. B., P. A. Rochford, and H. E. Hurlburt, 2000: An optimal definition for ocean mixed layer depth. *J. Geophys. Res.*, **105**, 16 803–16 821, https://doi.org/10.1029/2000JC900072.

Kuhlbrodt, T., J. M. Gregory, and L. C. Shaffrey, 2015: A process-based analysis of ocean heat uptake in an AOGCM with an eddy-permitting ocean component. *Climate Dyn.*, **45**, 3205–3226, https://doi.org/10.1007/s00382-015-2534-0.

——, and Coauthors, 2018: The low resolution version of HadGEM3 GC3.1: Development and evaluation for global climate. *J. Adv. Model. Earth Syst.*, **10**, 2865–2888, https://doi.org/10.1029/2018MS001370.

Lee, M.-M., A. C. Coward, and A. J. G. Nurser, 2002: Spurious diapycnal mixing of the deep waters in an eddy-permitting global ocean model. *J. Phys. Oceanogr.*, **32**, 1522–1535, https://doi.org/10.1175/1520-0485(2002)032<1522:SDMOTD>2.0.CO;2.

Liu, C., and R. P. Allan, 2022: Reconstructions of the radiation fluxes at the top of atmosphere and net surface energy flux: DEEP-C version 5.0. University of Reading, accessed 21 August 2022, https://doi.org/10.17864/1947.000347.

——, and Coauthors, 2015: Combining satellite observations and reanalysis energy transports to estimate global net surface energy fluxes. *J. Geophys. Res. Atmos.*, **120**, 9374–9389, https://doi.org/10.1002/2015JD023264.

——, and Coauthors, 2017: Evaluation of satellite and reanalysis-based global net surface energy flux and uncertainty estimates. *J. Geophys. Res. Atmos.*, **122**, 6250–6272, https://doi.org/10.1002/2017JD026616.

Luyten, J. R., J. Pedlosky, and H. Stommel, 1983: The ventilated thermocline. *J. Phys. Oceanogr.*, **13**, 292–309, https://doi.org/10.1175/1520-0485(1983)013<0292:TVT>2.0.CO;2.

Madec, G., and Coauthors, 2022: NEMO ocean engine, version 4.2.0. Scientific Notes of Climate Modelling Center 27, Institut Pierre-Simon Laplace, 323 pp., https://doi.org/10.5281/zenodo.1464816.

Marsh, R., 2000: Recent variability of the North Atlantic thermohaline circulation inferred from surface heat and freshwater fluxes. *J. Climate*, **13**, 3239–3260, https://doi.org/10.1175/1520-0442(2000)013,3239:RVOTNA.2.0.CO;2.

Marshall, D. P., and H. L. Johnson, 2013: Propagation of meridional circulation anomalies along western and eastern boundaries. *J. Phys. Oceanogr.*, **43**, 2699–2717, https://doi.org/10.1175/JPO-D-13-0134.1.

——, D. R. Munday, L. C. Allison, R. J. Hay, and H. L. Johnson, 2016: Gill's model of the Antarctic circumpolar current, revisited: The role of latitudinal variations in wind stress. *Ocean Modell.*, **97**, 37–51, https://doi.org/10.1016/j.ocemod.2015.11.010.

Mayer, M., L. Haimberger, J. M. Edwards, and P. Hyder, 2017: Toward consistent diagnostics of the coupled atmosphere and ocean energy budgets. *J. Climate*, **30**, 9225–9246, https://doi.org/10.1175/JCLI-D-17-0137.1.

McWilliams, J. C., G. Danabasoglu, and P. R. Gent, 1996: Tracer budgets in the warm water sphere. *Tellus*, **48A**, 179–192, https://doi.org/10.3402/tellusa.v48i1.12046.

Minobe, S., A. Kuwano-Yoshida, N. Komori, S.-P. Xie, and R. J. Small, 2008: Influence of the Gulf Stream on the troposphere. *Nature*, **452**, 206–209, https://doi.org/10.1038/nature06690.

Munday, D. R., H. L. Johnson, and D. P. Marshall, 2013: Eddy saturation of equilibrated circumpolar currents. *J. Phys. Oceanogr.*, **43**, 507–532, https://doi.org/10.1175/JPO-D-12-095.1.

Munk, W., and C. Wunsch, 1998: Abyssal recipes II: Energetics of tidal and wind mixing. *Deep-Sea Res. I*, **45**, 1977–2010, https://doi.org/10.1016/S0967-0637(98)00070-3.

Murtugudde, R., J. Beauchamp, C. R. McClain, M. Lewis, and A. J. Busalacchi, 2002: Effects of penetrative radiation on the upper tropical ocean circulation. *J. Climate*, **15**, 470–486, https://doi.org/10.1175/1520-0442(2002)015<0470:EOPROT>2.0.CO;2.

Nikurashin, M., and G. Vallis, 2011: A theory of deep stratification and overturning circulation in the ocean. *J. Phys. Oceanogr.*, **41**, 485–502, https://doi.org/10.1175/2010JPO4529.1.

Nilsson, J., D. Ferreira, T. Schneider, and R. C. J. Wills, 2021: Is the surface salinity difference between the Atlantic and Indo-Pacific a signature of the Atlantic meridional overturning circulation? *J. Phys. Oceanogr.*, **51**, 769–787, https://doi.org/10.1175/JPO-D-20-0126.1.

Nurser, A. J. G., and S. M. Griffies, 2019: Relating the diffusive salt flux just below the ocean surface to boundary freshwater and salt fluxes. *J. Phys. Oceanogr.*, **49**, 2365–2376, https://doi.org/10.1175/JPO-D-19-0037.1.

——, R. Marsh, and R. G. Williams, 1999: Diagnosing water mass formation from air-sea fluxes and surface mixing. *J. Phys. Oceanogr.*, **29**, 1468–1487, https://doi.org/10.1175/1520-0485(1999)029<1468:DWMFFA>2.0.CO;2.

Roberts, M. J., and Coauthors, 2019: Description of the resolution hierarchy of the global coupled HadGEM3-GC3.1 model as used in CMIP6 HighResMIP experiments. *Geosci. Model Dev.*, **12**, 4999–5028, https://doi.org/10.5194/gmd-12-4999-2019.

Roquet, F., G. Madec, T. J. McDougall, and P. M. Barker, 2015: Accurate polynomial expressions for the density and specific volume of seawater using the TEOS-10 standard. *Ocean Modell.*, **90**, 29–43, https://doi.org/10.1016/j.ocemod.2015.04.002.

Roullet, G., and G. Madec, 2000: Salt conservation, free surface, and varying levels: A new formulation for ocean general circulation models. *J. Geophys. Res.*, **105**, 23 927–23 942, https://doi.org/10.1029/2000JC900089.

Saenko, O. A., J. M. Gregory, S. M. Griffies, M. P. Couldrey, and F. B. Dias, 2021: Contribution of ocean physics and dynamics at different scales to heat uptake in low-resolution AOGCMs. *J. Climate*, **34**, 2017–2035, https://doi.org/10.1175/JCLI-D-20-0652.1.

Scaife, A. A., and Coauthors, 2011: Improved Atlantic winter blocking in a climate model. *Geophys. Res. Lett.*, **38**, L23703, https://doi.org/10.1029/2011GL049573.

Schloesser, F., R. Furue, J. P. McCreary, and A. Timmermann, 2012: Dynamics of the Atlantic meridional overturning circulation. Part 1: Buoyancy-forced response. *Prog. Oceanogr.*, **101**, 33–62, https://doi.org/10.1016/j.pocean.2012.01.002.

Simmons, H. L., S. R. Jayne, L. C. St. Laurent, and A. J. Weaver, 2004: Tidally driven mixing in a numerical model of the ocean general circulation. *Ocean Modell.*, **6**, 245–263, https://doi.org/10.1016/S1463-5003(03)00011-8.

Smith, R. D., M. E. Maltrud, F. Bryan, and M. W. Hecht, 2000: Numerical simulation of the North Atlantic Ocean at 1/10°. *J. Phys. Oceanogr.*, **30**, 1532–1561, https://doi.org/10.1175/1520-0485(2000)030<1532:NSOTNA>2.0.CO;2.

Srokosz, M., G. Danabasoglu, and M. Patterson, 2021: Atlantic meridional overturning circulation: Reviews of observational and modeling advances—An introduction. *J. Geophys. Res. Oceans*, **126**, e2020JC016745, https://doi.org/10.1029/2020JC016745.

Stommel, H., 1957: A survey of ocean current theory. *Deep-Sea Res.*, **4**, 149–184, https://doi.org/10.1016/0146-6313(56)90048-X.

Storkey, D., and Coauthors, 2018: UK global ocean GO6 and GO7: A traceable hierarchy of model resolutions. *Geosci. Model Dev.*, **11**, 3187–3213, https://doi.org/10.5194/gmd-11-3187-2018.

Talley, L. D., 2013: Closure of the global overturning circulation through the Indian, Pacific, and Southern Oceans: Schematics and transports. *Oceanography*, **26**, 80–97, https://doi.org/10.5670/oceanog.2013.07.

——, G. L. Pickard, W. J. Emery, and J. H. Swift, 2011: *Descriptive Physical Oceanography*. 6th ed. Elsevier, 555 pp.

Tamsitt, V., L. D. Talley, M. R. Mazloff, and I. Cerovecki, 2016: Zonal variations in the Southern ocean heat budget. *J. Climate*, **29**, 6563–6579, https://doi.org/10.1175/JCLI-D-15-0630.1.

——, R. P. Abernathey, M. R. Mazloff, J. Wang, and L. D. Talley, 2018: Transformation of deep water masses along Lagrangian upwelling pathways in the Southern Ocean. *J. Geophys. Res. Oceans*, **123**, 1994–2017, https://doi.org/10.1002/2017JC013409.

Vallis, G. K., 2017: *Atmospheric and Oceanic Fluid Dynamics*. 2nd ed. Cambridge University Press, 946 pp., https://doi.org/10.1017/9781107588417.

van Sebille, E., and Coauthors, 2018: Lagrangian ocean analysis: Fundamentals and practices. *Ocean Modell.*, **121**, 49–75, https://doi.org/10.1016/j.ocemod.2017.11.008.

von Storch, J.-S., C. Eden, I. Fast, H. Haak, D. Hernandez-Deckers, E. Maier-Reimer, J. Marotzke, and D. Stammer, 2012: An estimate of the Lorenz energy cycle for the world ocean based on the 1/10° STORM/NCEP simulation. *J. Phys. Oceanogr.*, **42**, 2185–2205, https://doi.org/10.1175/JPO-D-12-079.1.

Walin, G., 1982: On the relation between sea-surface heat flow and thermal circulation in the ocean. *Tellus*, **34**, 187–195, https://doi.org/10.3402/tellusa.v34i2.10801.

Zemskova, V. E., B. L. White, and A. Scotti, 2015: Available potential energy and the general circulation: Partitioning wind, buoyancy forcing, and diapycnal mixing. *J. Phys. Oceanogr.*, **45**, 1510–1531, https://doi.org/10.1175/JPO-D-14-0043.1.